

1 **Differential growth and transcriptomic profile of stem cell-**
2 **derived midbrain astrocytes**

3 Zongze Li^{1&2}, Lucia Fernandez Cardo¹, Michal Rokicki¹, Jimena Monzón-Sandoval¹,
4 Viola Volpato¹, Frank Wessely¹, Caleb Webber^{1*}, Meng 89Li^{2*}

5 ¹ Dementia Research Institute, School of Medicine, Cardiff University, Hadyn Ellis
6 Building, Maindy Road, Cardiff, CF24 4HQ, UK

7 ² Neuroscience and Mental Health Innovation Institute, School of Medicine, Cardiff
8 University, Hadyn Ellis Building, Maindy Road, Cardiff, CF24 4HQ, UK

9

10 *Corresponding authors:

11 Meng Li, lim26@cardiff.ac.uk,

12 Caleb Webber, webberc4@cardiff.ac.uk

13

14 Key words: astrocyte, regional heterogeneity, ventral midbrain, dopaminergic, single
15 cell RNA-sequencing

16 **Abstract**

17 Regional specificity of stem cell-derived astrocytes is believed to be an important
18 prerequisite for their applications in disease modelling and cell-based therapies. The
19 regional identity of these astrocytes is often defined by the positional characteristics
20 of their antecedent, stem cell-derived neural progenitors patterned to a fate of
21 interest, with the assumption that the positional specification is to be preserved by
22 the derived astrocytes. Using a human induced pluripotent stem cell line designed
23 for tracing midbrain floor plate derivatives, here we show that lineage composition of
24 the derived astrocytes is not a faithful recapitulation of the founder progenitor
25 population, as demonstrated by the loss of floor plate differentiated progeny in the
26 final astrocyte products. Using deep single cell RNA sequencing, we identified
27 distinct transcriptomic signatures of midbrain floor plate-derived astrocytes. Our
28 study highlights the need for rigorous characterisation of pluripotent stem cell-
29 derived regional astrocytes and provides a valuable resource for assessing midbrain
30 floor plate-derived human astrocytes.

31 Introduction

32 Astrocytes are the most abundant cells in the brain. They play important roles in the
33 central nervous system in supporting neuronal survival and synaptic activities,
34 including the regulation of ionic homeostasis, providing energetic support, elimination
35 of oxidative stress, and neurotransmitter removal and recycle (Verkhratsky and
36 Nedergaard 2018). Abnormalities in astrocytes have been linked to various
37 neurodegenerative and neurodevelopmental disorders, such as Parkinson's disease,
38 Alzheimer's disease, Huntington's disease, autism spectrum disorders and
39 Alexander's disease (Molofsky et al. 2012; Phatnani and Maniatis 2015; Booth et al.
40 2017). There is therefore a growing interest in using human pluripotent stem cell
41 (PSC)-derived astrocytes for disease modelling *in vitro* (Chandrasekaran et al. 2016).

42 Contrary to the widely held belief that astrocytes in the brain are largely identical,
43 recent studies revealed diversity in their transcriptomic profile, physiological properties
44 and function (Oberheim et al. 2009; Schober et al. 2022). For example, single cell and
45 spatial transcriptomic studies have identified several astrocyte subpopulations in the
46 mouse cortex (Zhu et al. 2018; Batiuk et al. 2020; Bayraktar et al. 2020). In human,
47 although astrocyte heterogeneity remains largely elusive, heterogeneity in radial glia
48 across brain regions and within midbrain has been reported (La Manno et al. 2016; Li
49 et al. 2023). Furthermore, different molecular and physiological features and distinct
50 responses to stimuli were also observed in astrocytes from different mouse brain
51 regions (Takata and Hirase 2008; Chai et al. 2017; Morel et al. 2017; Itoh et al. 2018;
52 Kostuk et al. 2019; Makarava et al. 2019; Xin et al. 2019; Lozzi et al. 2020). Indeed,
53 astrocyte heterogeneity has been suggested to underly the regional susceptibility to
54 human diseases (Schober et al. 2022). Therefore, recapitulating astrocyte regional
55 specificity in PSC-derived astrocytes is generally accepted as an important
56 prerequisite.

57 Several reports have described the generation of regional astrocytes from human
58 embryonic stem cells or induced pluripotent stem cells (iPSCs) which include forebrain
59 (Krencik et al. 2011; Zhou et al. 2016; Tcw et al. 2017; Lin et al. 2018; Bradley et al.
60 2019; Hedegaard et al. 2020; Peteri et al. 2021), ventral midbrain (Booth et al. 2019;
61 Barbuti et al. 2020; Crompton et al. 2021; de Rus Jacquet et al. 2021), hindbrain and

62 spinal cord (Roybon et al. 2013; Serio et al. 2013; Holmqvist et al. 2015; Bradley et al.
63 2019; di Domenico et al. 2019; Yun et al. 2019). The regional identity of these
64 astrocytes is typically evaluated at the stage of early neural progenitors generated via
65 cell type- or region-directed neural patterning protocols, with the assumption that the
66 positional characteristics will be faithfully preserved in the final astrocyte products.
67 However, astrocyte production in vitro involves an extended period of astrocytic fate
68 induction and progenitor expansion using FGF and EGF while substantial literature
69 reported alterations in region-specific gene expression and/or neurogenic competence
70 in expanded neural progenitors (Jain et al. 2003; Sun et al. 2008; Koch et al. 2009;
71 Falk et al. 2012). Therefore, better characterisations of PSC-derived astrocytes and
72 their lineage-specific features are needed to advance our knowledge about the
73 molecular heterogeneity of human astrocytes.

74 Using a human iPSC line that allows the tracing of LMX1A expressing midbrain floor
75 plate neural progenitors and their differentiated progeny (Cardo et al. 2023), we
76 discovered an unexpected gradual depletion of LMX1A⁺ progenitor progeny during
77 astrocyte induction from a bulk population of ventral midbrain patterned progenitors
78 despite LMX1A⁺ progenitors being the predominant starting population. LMX1A⁺
79 progenitor derived astrocytes can however be generated if astrocytic induction is
80 initiated from purified LMX1A⁺ progenitors, indicating that the positional constituents
81 of the founding cell population may not be preserved faithfully in the derived
82 astrocytes. Single cell RNA sequencing (scRNAseq) of astrocytes derived from both
83 parental populations identified distinct transcriptomic signatures, providing a useful
84 resource for assessment of human PSC-derived midbrain astrocytes.

85 **Results**

86 **Depletion of LMX1A⁺ progenitors and/or derivatives in ventral** 87 **midbrain patterned neural progenitor cultures during astrogenic** 88 **induction**

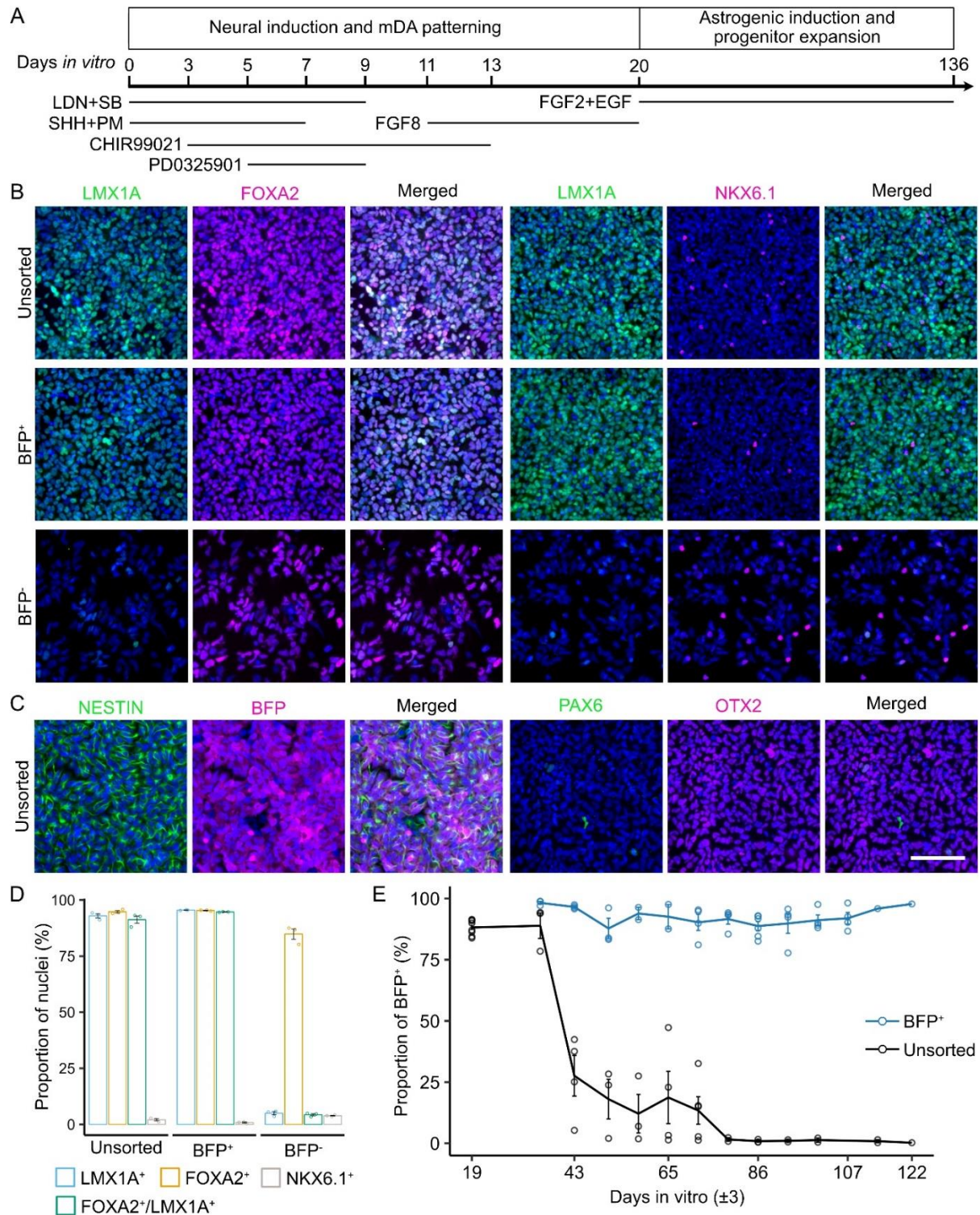
89 To investigate whether regionally patterned neural progenitors retain their lineage
90 identity during astrogenic induction and glial progenitor expansion, we made use of

91 the LMX1A-Cre/AAVS1-BFP iPSCs tracer line, which enables the tracking of LMX1A⁺
92 midbrain floor plate progenitors and their differentiated progeny (Cardo et al. 2023)^[OBJ].
93 We differentiated the LMX1A-Cre/AAVS1-BFP iPSCs towards the ventral midbrain
94 fate following a modified protocol based on Jaeger *et al.* and Nolbrant *et al.* (Jaeger et
95 al. 2011; Nolbrant et al. 2017)^[OBJ] (Figure 1A). Immunocytochemistry of day (d)19
96 cultures confirmed a high proportion of cells expressing BFP (96.01±0.42%) and
97 ventral midbrain progenitor markers LMX1A (92.94±0.91%), FOXA2 (94.76±0.57%)
98 and OTX2 (97.82±0.28%; Figure 1B-D with the original images shown in Figure S1A).
99 Most cells (91.26±1.64%) co-expressed LMX1A and FOXA2 (Figure 1B and 1D). At
100 this stage, all BFP⁺ cells also stained positive to a pan neural progenitor marker
101 NESTIN (Figure 1C). We detected a small proportion of cells expressing midbrain
102 basal plate marker NKX6.1 (2.03±0.47%, Figure 1B-C) whose expression domain in
103 the early developing ventral midbrain partially overlap with that of (Andersson et al.
104 2006) (Andersson et al. 2006)^[OBJ]. However, few PAX6⁺ cells were present (Figure 1C),
105 which marks the forebrain and (Duan et al. 2013) (Duan et al. 2013)^[OBJ].
106 Immunocytochemical analysis of FACS-sorted BFP⁺ cells confirmed highly enriched
107 expression of LMX1A (95.51±0.09%) and FOXA2 (95.35±0.14%), and co-expression
108 of both markers (94.68±0.10%; Figure 1B and 1D). In contrast, only a small number
109 of LMX1A⁺ cells (4.96±0.70%) were present in the sorted BFP⁻ population (Figure 1B
110 and 1D). These findings provide further support that BFP expression faithfully
111 recapitulate LMX1A expression and that LMX1A⁺ ventral midbrain progenitors
112 represent the major cell population in d19 (Cardo et al. 2023) (Cardo et al. 2023)^[OBJ].

113 The d19 cells were then induced to undergo astrogenic switch in media containing
114 FGF2 and EGF with the BFP content monitored by flow cytometry at each weekly
115 passaging (Figure 1A, representative gating strategy is shown in Figure S1B-E). We
116 found, unexpectedly, a dramatic decrease of BFP⁺ cell proportion from the starting
117 point of 88.20±1.10% to only 27.59±8.28% at d43 and to nearly absent as the
118 differentiation continued (Figure 1E). We did not observe evident cell death during
119 culture and replating; thus, the absence of BFP could be either due to the silencing of
120 BFP expression in the derivatives of LMX1A⁺ progenitors or the loss of these cells
121 through growth competition. To address this question, we performed progenitor
122 expansion and astrogenic induction under the same culture condition with purified d19

123 BFP⁺ progenitors isolated using fluorescence-activated cell sorting (FACS).
124 Interestingly, the sorted BFP⁺ cells exhibited similar population growth rate to that of
125 unsorted cultures, and the proportion of BFP⁺ cells remained at approximately 90%
126 throughout the astrogenic induction and glial progenitor expansion period (Figure 1E).
127 This observation demonstrates that BFP expression can be maintained in the
128 derivatives of LMX1A⁺ midbrain floorplate progenitors, and that the loss of BFP⁺ cells
129 in the unsorted culture is likely due to their growth disadvantage compared to the
130 derivatives of LMX1A⁻ progenitors.

131 Our finding is unexpected and demonstrates that the regional or lineage identity of
132 PSC-derived astrocytic cells should not be assumed merely based on the dominant
133 regional property of their cellular origin, given that no *in vitro* fate specification
134 paradigm is 100% efficient.



135

136

137

138

139

140

141

142

Figure 1. Depletion of LMX1A⁺ progenitors and their derivatives during astrogenic induction in ventral midbrain patterned neural progenitor cultures.

A, Schematic diagram of ventral midbrain neural differentiation and astrogenic induction. B-C, Representative view of immunocytochemistry of ventral midbrain neural progenitor markers and other regional markers in d19 unsorted, sorted BFP⁺, and sorted BFP⁻ population. Scale bar represents 100 μ m. Images shown were cropped to 300 μ m \times 300 μ m by randomly selecting the region of interest in the nuclei-

143 only channel (uncropped greyscale images are shown in Figure S1A). D,
144 Quantification of marker expression in unsorted, sorted BFP⁺, and sorted BFP⁻
145 population. Error bars represent the standard error of means (SEM) of three
146 independent experiments. E, Flow cytometry quantification of unsorted and BFP⁺
147 population during astrogenic induction and progenitor expansion. Each data point
148 represents one biological replicate. The gating strategy used is shown in Figure S1B.

149

150 **Astrogenic switch occurred earlier in derivatives of LMX1A⁺** 151 **midbrain progenitors.**

152 Since sorted BFP⁺ (LMX1A⁺ or their derivatives) and unsorted astrocytic cultures differ
153 distinctively in BFP expression soon after the initiation of astrogenic induction, for
154 simplicity, these cultures are hereafter referred to as the BFP⁺ and BFP⁻ cultures,
155 respectively. Wondering whether the two cell populations behave differently in the
156 process of astrogenic switch, we examined astrocytic marker expression in these
157 cultures at d45 and d98 by immunocytochemistry. SOX9 and NFIA are transcription
158 factors crucial for the initiation of astrogenesis and acquisition of astrogenic
159 competence in the developing central nervous system (Stolt et al. 2003; Deneen et al.
160 2006), while CD44 identifies astrocyte-restricted precursors (Liu et al. 2004). We found
161 that all these markers were more abundantly detected in the BFP⁺ cultures (NFIA:
162 65.89±2.81%; SOX9: 57.19±4.25%) than the BFP⁻ cultures (NFIA: 4.26±1.28%; SOX9:
163 8.88±1.82%) at d45 (Two-way ANOVA with post-hoc Turkey test, NFIA: $p=2.52\times 10^{-5}$,
164 SOX9: $p=9.21\times 10^{-6}$; Figure 2A-B with the original images shown in Figure S2).
165 Although the number of NFIA⁺ and SOX9⁺ cells significantly increased in the BFP⁻
166 cultures by d98 (NFIA: 44.07±4.56% on d98, $p=3.58\times 10^{-4}$; SOX9: 44.28±2.84% on
167 d98, $p=1.21\times 10^{-4}$), the BFP⁺ cultures still contained more cells expressing NFIA
168 (65.71±4.25%; $p=2.06\times 10^{-2}$) and SOX9 (73.25±2.12%; $p=5.51\times 10^{-4}$) than BFP⁻
169 cultures (Figure 2A and 2C).

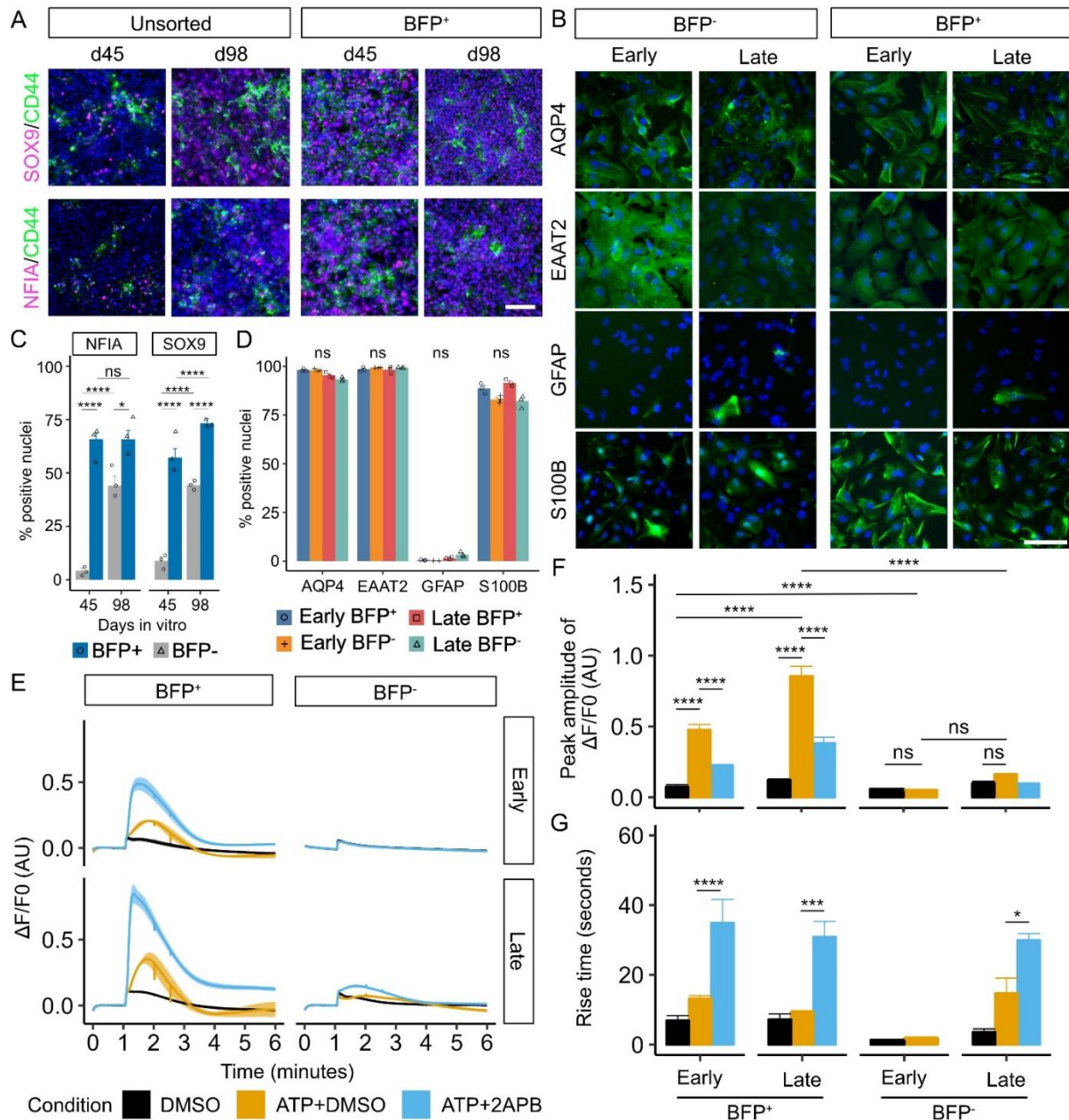
170 To investigate whether the temporal difference in astrocytic switch between the BFP⁺
171 and BFP⁻ cultures affects maturation and functionality of the derived astrocytes, we
172 initiated astrocyte terminal differentiation by exposing the BFP⁺ and BFP⁻ astrocyte
173 precursors to CNTF and BMP4 (Krencik et al. 2011; Bradley et al. 2019) from d87
174 (referred to as early astrocytes) and d136 (late astrocytes). Both BFP⁺ and BFP⁻

175 cultures exhibited a similar expression profile of classic astrocyte markers, including
176 AQP4, EAAT2, and S100B, but few GFAP⁺ cells at both time points (Figure 2B and
177 2D with the original images shown in Figure S3).

178 As a reference, we also generated neural progenitors without employing any
179 patterning cues and induced astrogenic switch and astrocyte differentiation from these
180 non-patterned neural progenitors (Figure S4A-B). We found that, while the astrocyte
181 cultures derived from the non-patterned progenitors contained a similar proportion of
182 cells expressing AQP4, EAAT2 and S100B compared to the BFP⁺ and BFP⁻ astrocyte
183 cultures, there are more GFAP⁺ cells in the non-patterned astrocyte preparations
184 (17.89±5.4%, Figure S4A-B).

185 Functional astrocytes exhibit transient calcium (Ca²⁺) spikes upon chemical
186 stimulation, such as ATP (Zhang et al. 2016). Using a FLIPR Ca²⁺ release assay, we
187 observed a sharp increase in the intracellular Ca²⁺ concentration upon ATP
188 administration in both the early and late BFP⁺ astrocyte populations (early BFP⁺:
189 $p=5.37 \times 10^{-12}$; late BFP⁺: $p<2.2 \times 10^{-16}$; Figure 2E-F). ATP induced Ca²⁺ release is
190 partially mediated by inositol trisphosphate. Indeed, addition of an inositol
191 trisphosphate receptor antagonist 2-aminoethoxydiphenylborate (2-APB) reduced the
192 amplitude (early BFP⁺: $p=5.88 \times 10^{-5}$; late BFP⁺: $p=9.22 \times 10^{-10}$; Figure 2F) and rise time
193 (early BFP⁺: $p=2.63 \times 10^{-5}$; late BFP⁺: $p=3.59 \times 10^{-4}$; late BFP⁻: $p=0.028$; Figure 2G) of
194 ATP-induced Ca²⁺ response in both the early and late BFP⁺ astrocytes. Interestingly,
195 the early BFP⁺ astrocytes had significantly lower peak amplitude than that observed
196 in late BFP⁺ astrocytes ($p=6.92 \times 10^{-9}$; Figure 2F), despite their similar level of astrocyte
197 marker expression, suggesting a difference in maturity at the functional level. Early
198 and late BFP⁻ astrocytes exhibited a similar profile of time-dependent increase in the
199 amplitude of ATP-induced Ca²⁺ response but did not reach statistical significance
200 (Figure 2E-F). However, late BFP⁻ astrocytes showed a significantly lower peak
201 amplitude than late BFP⁺ astrocytes ($p<2.2 \times 10^{-16}$; Figure 2E-F).

202 Taken together, our data demonstrate that astrogenesis occurred earlier in BFP⁺
203 cultures than BFP⁻ cells. This temporal difference is also reflected in functional maturity
204 of the derived astrocytes, despite a similar expression profile of classic astroglial
205 markers.



206

207

208

209

210

211

212

213

214

215

216

217

218

219

220 performed to compare between lineages (NFIA: $p=5.389 \times 10^{-6}$, $df=1$, effect size=3.62;
221 SOX9: $p=1.96 \times 10^{-6}$, $df=1$, effect size=4.77) and days of differentiation (NFIA:
222 $p=7.82 \times 10^{-5}$, $df=1$, effect size=1.99; SOX9: $p=2.62 \times 10^{-5}$, $df=1$, effect size=2.99) D,
223 Quantification of immunocytochemistry of astrocyte marker expression in astrocytes.
224 Error bars represent SEM of three independent experiments. Kruskal-Wallis test
225 results following Bonferroni correction are shown on the top of the figure (AQP4:
226 $p.adjust=0.12$, $df=3$, $H=8.95$; EAAT2: $p.adjust=1.00$, $df=3$, $H=0.95$; GFAP:
227 $p.adjust=0.06$, $df=3$, $H=10.38$; S100B: $p.adjust=0.11$, $df=3$, $H=9.05$). E, Averaged
228 trace of ATP-induced Ca^{2+} response assayed using FLIPR. Drugs or DMSO were
229 applied at 1 minute of the assay. The line represents the average fluorescence change
230 ($\Delta F/F_0$) in at least three independent experiments each with at least three replicate
231 wells. The shaded area represents the SEM across at least three independent
232 experiments. F, Quantitative comparison of the peak amplitude of ATP-induced Ca^{2+}
233 response among conditions (two-way ANOVA, $p < 2.2 \times 10^{-16}$, $df=2$, effect size=2.54)
234 and samples ($p=2.87 \times 10^{-14}$, $df=3$, effect size=2.17). Error bars represent the SEM
235 across at least independent experiments. G: Quantitative comparison of the rise time
236 of ATP-induced Ca^{2+} response among conditions (two-way ANOVA, $p=2.19 \times 10^{-13}$,
237 $df=2$, effect size =1.958) and samples ($p=0.064$, $df=3$, effect size=0.76). Intergroup
238 comparison was performed using Post-hoc Tukey test. Error bars represent the SEM
239 across at least three independent experiments. (****: $p < 0.0001$, ***: $p < 0.001$, **: $p < 0.01$, *: $p < 0.05$, ns: not significant).
240

241

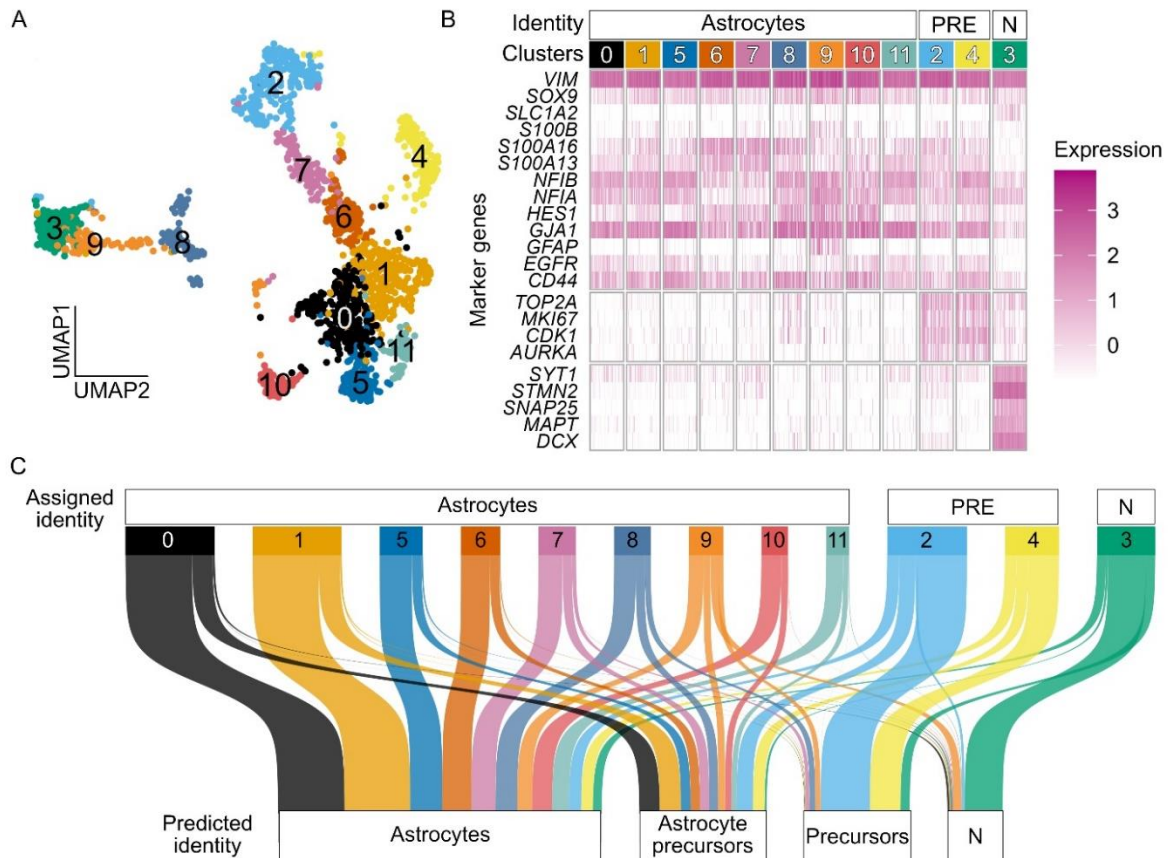
242 **Single cell RNA sequencing confirms the authenticity of PSC-** 243 **derived astrocytes.**

244 To further characterize the PSC-derived astrocytes, we performed full-length
245 scRNAseq on early and late BFP⁺ and BFP⁻ astrocytes using the iCELL8 platform and
246 SMART-seq technology, with non-patterned astrocytes derived from the LMX1A-
247 Cre/AAVS1-BFP tracer line as a control. A sample of iPSC-derived neurons was
248 included to facilitate downstream cell type identification. We profiled FACS purified
249 astrocytes expressing CD49f as well as unsorted cultures for comparison of all three
250 astrocyte populations (Barbar et al. 2020); Figure S4C-H). After stringent filtering
251 (Figure S5A-C, see Methods and Materials on filtering), we obtained a total of 17478
252 protein-coding genes in 1786 qualifying cells, with an average of 6326 protein-coding
253 genes detected per cell.

254 Unsupervised Louvain clustering identified 12 cell clusters (Figure 3A). Cells clustered
255 mainly based on sample type (astrocytes and neurons; Figure S6A) and the estimated
256 cell cycle phase (Figure S6B), while sorted CD49f⁺ and unsorted astrocytes were

257 clustered together (Figure S6A). *TagBFP* was detected at a higher level in BFP⁺
258 astrocyte samples than in BFP⁻ and NP samples, while *TagBFP* expression was
259 negligible in the neuronal samples derived from an iPSC line without BFP transgene
260 (Figure S6C-D). Using a set of known astrocyte and neuronal signature genes (Figure
261 3B), we identified cells in clusters 0, 1, and 5-11 as astrocytes (Figure 3B), which were
262 enriched in expression of *SOX9*, *NFIA*, *NFIB*, *HES1*, *S100A13*, *S100A16*, *EGFR*,
263 *CD44* and *GJA1* (Figure 3B). These transcripts were also detected at high levels in
264 clusters 2 and 4, which were mostly estimated to be in cell cycle phases G2, M and S
265 (Figure S6B). In addition, clusters 2 and 4 showed high levels of proliferation-related
266 transcripts, such as *TOP2A*, *MKI67*, *CDK1* and *AURKA* (Figure 3B), and are thus
267 defined as astrocyte precursors. In contrast, Cluster 3 contains mostly cells from the
268 neuronal sample (Figure 3A and Figure S6A) and indeed expressed high levels of
269 genes closely related to neuronal structure and function (such as *STMN2*, *SYT1*, *DCX*,
270 *MAPT*, and *SNAP25*; Figure 3B). We did not detect transcripts indicative of endoderm
271 (*GATA4*), mesoderm (*TBXT* and *TBX6*), and oligodendrocyte progenitors (*SOX10* and
272 *PDGFRA*) in any of these clusters (Figure S6C).

273 To determine the authenticity of these PSC-derived astrocytes, we mapped our data
274 to published scRNAseq datasets obtained from five foetal, an adult human brain and
275 a PSC-derived astrocyte study using Seurat integration (La Manno et al. 2016; Sloan
276 et al. 2017; Zhong et al. 2018; Polioudakis et al. 2019; Agarwal et al. 2020; Fan et al.
277 2020; Bhaduri et al. 2021; Eze et al. 2021). We found that cells in clusters annotated
278 as astrocytes (clusters 0, 1, and 5-11) were indeed predominantly mapped to the
279 reference astrocyte or astrocyte precursor populations with high confidence
280 (prediction score over 0.5; Figure 3C and Figure S7). In contrast, neuronal cluster 2
281 was mapped to neurons of the foetal reference datasets, while the astrocyte precursor
282 clusters (2 and 4) were mapped to progenitor populations in the foetal reference
283 datasets (Figure 3C and Figure S7). These findings demonstrate that our iPSC-
284 derived astrocytes closely resemble those in the human brains.



285

286 **Figure 3. Single cell RNA sequencing confirms the authenticity of PSC-derived**
 287 **astrocytes.**

288 A, Uniform manifold approximation and projection plot of unbiased clustering, coloured
 289 by clusters. B, Heatmap of the normalised expression of selected markers in different
 290 clusters. The assigned identity to each cluster is shown at the top of the plot. C, Sankey
 291 plot summarising the result of reference mapping of cells in different clusters to eight
 292 published reference human brain scRNAseq datasets. The thickness of the thread is
 293 proportional to the number of cells mapped to the same identity in the reference
 294 datasets (predicted identity). Detailed results of referencing mapping to each reference
 295 datasets are shown in Figure S7A-H and prediction score shown in Figure S7I. (PRE:
 296 precursors; N: neurons)

297

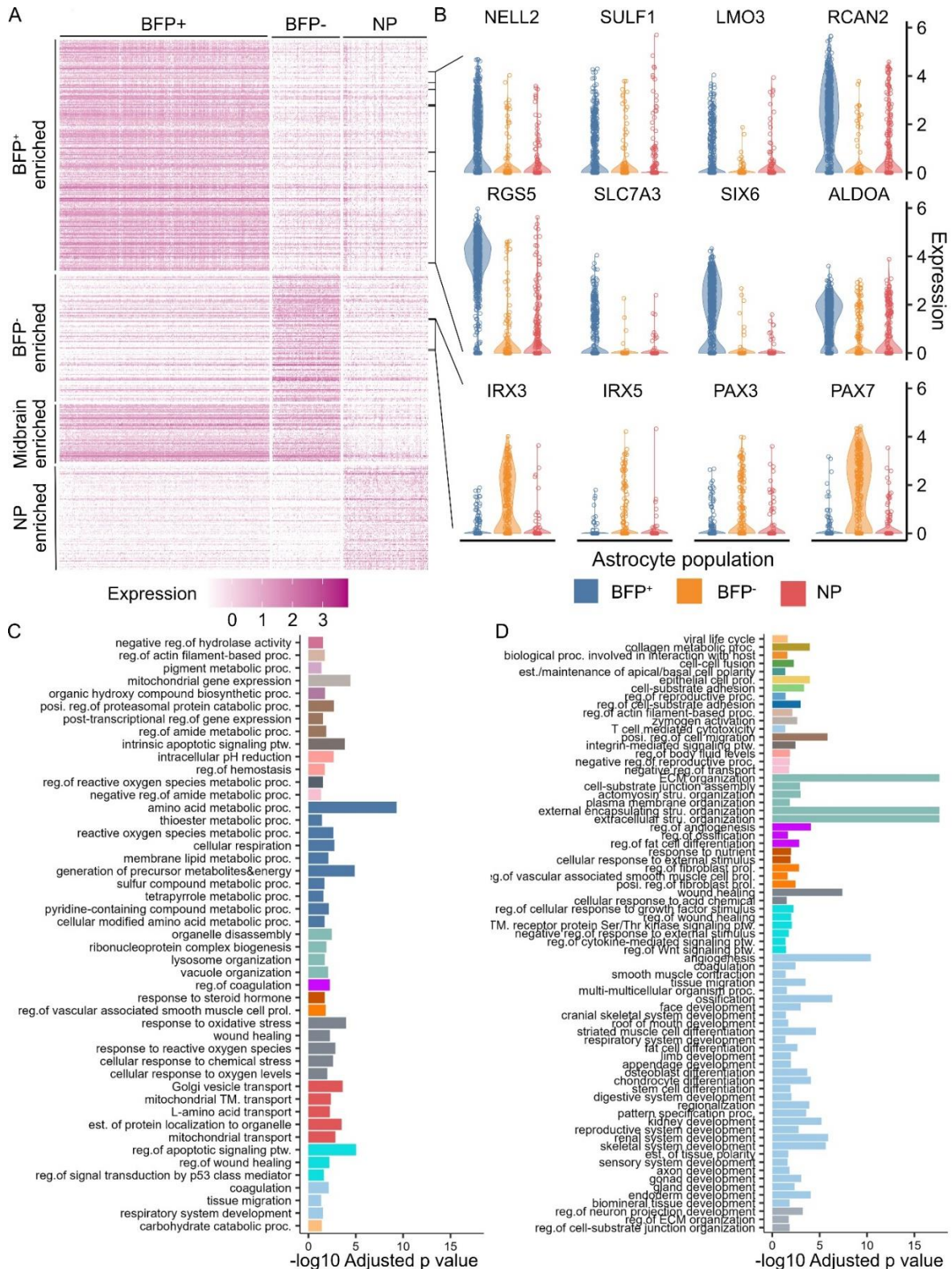
298 **Distinct transcriptome fingerprints of LMX1A⁺ midbrain floor plate-**
 299 **derived astrocytes**

300 Significant advance has been made recently in understanding the molecular profiles
 301 of midbrain dopamine neurons. However, our knowledge about midbrain astrocytes in
 302 this regard remains limited and does not inform anatomic or lineage origin of the cells.

303 In this regard, the BFP⁺ astrocytes provide a unique resource to determine the
304 transcriptomic characteristics of human midbrain floor plate derived astrocytes. By
305 performing pairwise differential gene expression (details described in Methods and
306 Materials), we identified 1153 genes differentially expressed (DEGs; adjusted p values
307 less than 0.05 and log₂ fold change over 0.25) in BFP⁺ astrocytes when compared to
308 either BFP⁻ or non-patterned astrocyte populations (Supplementary Data 1). Of these,
309 159 were unique to BFP⁺ astrocytes (BFP⁺ enriched, Figure 4A), which include genes
310 associated with midbrain dopamine neuron development such as *SULF1*, *LMO3*,
311 *NELL2*, and *RCAN2* (Figure 4B) (Strelau et al. 2000; La Manno et al. 2016; Bifsha et
312 al. 2017; Ahmed et al. 2021). Interestingly, *LMX1A* and *FOXA2*, which was used to
313 evaluate PSC-derived midbrain astrocytes in previous studies, were not detected in
314 BFP⁺ astrocytes (Figure S6D). We also identified 530 DEGs enriched in BFP⁻
315 astrocytes only (BFP⁻ enriched, Figure 4A and Supplementary Data 1), which include
316 those known to be expressed in the ventrolateral - dorsal domain of the midbrain and
317 hindbrain, such as *IRX3*, *IRX5*, *PAX3*, and *PAX7* (Figure 4B)(Houweling et al. 2001;
318 Matsunaga et al. 2001). This transcription profile supports the notion that the BFP⁻
319 astrocytes are descendants of the initial minor populations of lateral midbrain
320 progenitors. Moreover, 72 DEGs were shared by BFP⁺ and BFP⁻ astrocytes against
321 the non-patterned astrocytes (midbrain enriched, Figure 4A and Supplementary Data
322 1). This set of genes includes *NR2F1*, *NR2F2*, *ZEB2*, *KCNJ6* and *SRPX* (Figure 4B),
323 which have been reported to be signatures of mouse midbrain astrocytes (Endo et al.
324 2022). Together, our findings provide a new entry to transcriptomic characteristics of
325 midbrain astrocytes and specifically a gene expression map of midbrain floor plate
326 derived human astrocyte lineage.

327 Gene ontology (GO) enrichment analysis was performed on the 1153 DEGs enriched
328 in BFP⁺ astrocytes (Supplementary Data 2). The significantly enriched GO terms were
329 mainly related to various aspects of metabolism, stress response, biosynthesis,
330 lysosomal activity, and cellular respiration (Figure 4C and Supplementary Data 3).
331 These biological processes have previously been shown to be disrupted by several
332 mutations causing familial Parkinson's disease (di Domenico et al. 2019; Barbuti et al.
333 2020; Sonninen et al. 2020). In contrast, the GO terms associated with 530 BFP⁻
334 astrocyte enriched DEGs were mostly related to formation of extracellular matrix and

335 tissue development (Figure 4D and Supplementary Data 2-3). The differential
 336 enrichment of GO terms implicates functional difference between the BFP⁺ and BFP⁻
 337 astrocytes and supports the need for generating regional specific astrocytes for
 338 disease modelling.



339

340 **Figure 4. Distinct transcriptome fingerprints of LMX1A⁺ midbrain floor plate-**
341 **derived astrocytes**

342 A, Heatmap of the normalised expression of population-specific genes in different
343 populations of astrocytes. B, Violin plots of the normalised expression of selected
344 candidate markers for BFP⁺, BFP⁻, and non-patterned (NP) astrocytes. C-D,
345 Representative GO terms significantly enriched in BFP⁺ (C) and BFP⁻ (D) enriched
346 genes. Semantically similar representative terms were shown with the same colour.

347

348 **Discussion**

349 Despite the general belief that recapitulating astrocyte lineage heterogeneity is
350 necessary for stem cell-based disease modelling and cell transplantation, the extent
351 of astrocyte heterogeneity in different brain regions and subregions remains largely
352 elusive. By harnessing an LMX1A based lineage tracing human iPSC line and cutting
353 edge scRNAseq technology, we show that astrocytes derived from the LMX1A⁺
354 midbrain floor plate progenitors, the same cells giving rise to midbrain dopaminergic
355 neurons, possess distinct transcriptional landmarks from those derived from non-
356 midbrain patterned neural progenitors as well as other midbrain patterned progenitors.
357 Moreover, we discovered unexpected negative selection against derivatives of
358 LMX1A⁺ progenitors during astrocyte induction and progenitor expansion. Our study
359 highlights the need for careful characterisation of PSC-derived astrocytes and
360 provides a transcriptomic fingerprint for midbrain floor plate derived astrocytes.

361 Using a popular astrocyte in vitro differentiation paradigm, we found that astrocytes
362 descended from the LMX1A⁺ midbrain progenitors could only be obtained from purified
363 progenitors. In contrast, astrocytes derived from bulk midbrain patterned progenitors
364 exhibits transcriptomic profiles of the lateral-dorsal midbrain, despite LMX1A⁺ midbrain
365 progenitors being the predominant starting population. Our findings demonstrate that
366 the lineage composition of the parent progenitors may not be faithfully preserved
367 during astrocyte induction and progenitor expansion. FGF is the most popular
368 inductive molecule used for astrocyte differentiation from stem cells (Chandrasekaran
369 et al. 2016). It is evident however that FGF expanded neural progenitors, originated
370 either from the brain or neutralized PSCs, exhibit restricted regional competence and

371 positional gene expression. For example, bulk expanded human ventral midbrain
372 neural progenitors (Jain et al. 2003), and fetal forebrain or spinal cord derived neural
373 stem (NS) cells only give rise to GABAergic neurons (Sun et al. 2008); likewise, It-
374 NES cells display anterior hindbrain-like positional profile (Falk et al. 2012), while their
375 antecedents, PSC-derived neural rosettes and early passage derivatives, express
376 anterior forebrain markers (Koch et al. 2009). It is not clear whether this is due to
377 deregulation of the original patterning at the level of gene expression or the loss of
378 associated cell population (Gabay et al. 2003). In this study, since BFP⁺ astrocytes
379 can be generated under the same culture condition with purified LMX1A⁺ progenitors,
380 we reasoned that the loss of their derivatives in unsorted cultures was possibly due to
381 differential growth capacity.

382 Our study highlights the need for careful assessment of astrocyte positional identity.
383 A common practice in this regard is to confirm the regional characteristics of the
384 founder progenitors following fate directed neural induction, with the assumption that
385 the dominant positional features will be maintained by the astrocyte progeny (Krencik
386 et al. 2011). This strategy is at least partly dictated by our limited knowledge in gene
387 expression signatures of regional- and/or lineage-specific astrocytes. Hence, an end
388 point evaluation of PSC-derived astrocytes often relies on region-specific markers
389 defined in the developmental brain during the neurogenic period. For example, LMX1A
390 and FOXA2 expression were used as criteria for midbrain astrocytes in previous
391 studies (Barbuti et al. 2020; Crompton et al. 2023). However, scRNAseq of human
392 fetal ventral midbrain and adult substantia nigra revealed negligible expression of
393 these transcripts in astrocytes (La Manno et al. 2016; Agarwal et al. 2020; Kamath et
394 al. 2022). Consistent with these findings, we did not detect LMX1A or FOXA2 in neither
395 the BFP⁺ nor BFP⁻ astrocytes. Our analysis however identified new positive and
396 negative markers that could be applied to confirm the regional identity of ventral
397 midbrain astrocytes.

398 In addition to distinct transcriptomic profile, BFP⁺ and BFP⁻ astrocytes may also be
399 functionally different. Astrocytes generated from progenitors broadly patterned to the
400 dorsal forebrain, ventral forebrain and spinal cord have been shown to exhibiting
401 different GO enrichment profile as well as different physiological and functional
402 properties (Bradley et al. 2019). In comparison to the BFP⁻ and non-patterned

403 astrocytes, the current study revealed that GO terms enriched in BFP⁺ astrocytes,
404 which originated from the same progenitor giving rise to midbrain dopaminergic
405 neurons, were closely related to various biological processes disrupted in astrocytes
406 carrying familial Parkinson's disease mutations (di Domenico et al. 2019; Barbuti et al.
407 2020; Sonninen et al. 2020). Such a distinct enrichment profile implicates BFP⁺
408 astrocytes being functionally adapted to supporting midbrain dopaminergic neurons
409 compared to BFP⁻ and non-patterned astrocytes.

410 In conclusion, this study lends further support on regional diversity of astrocytes and
411 identified a set of midbrain enriched genes. Crucially, the transcriptomic fingerprint of
412 human midbrain floor plate-derived astrocytes described here offers a much-needed
413 resource for assessing the authenticity of stem cell derived astrocytes in studies
414 associated with Parkinson's disease.

415 **Methods and Materials**

416 **Stem cell culture and astrocyte differentiation**

417 KOLF2 human iPSCs were maintained in E8 flex media (ThermoFisher) and manually
418 dissociated using Gentle Cell Dissociation Reagent (STEMCELL Technologies) as
419 previously described (Cardo et al. 2023). Astrocytes were differentiated using a three-
420 stage stepwise strategy consisting neural induction and regional patterning, astrogenic
421 switch and progenitor expansion, and astrocyte terminal differentiation. Midbrain floor
422 plate progenitors were generated as previously described (Cardo et al. 2023). At day
423 19, cells were replated as single cells onto poly-D-lysine-laminin-coated plates at
424 1×10^6 cells/cm² for astrogenic switch and progenitor expansion in N2B27 media
425 supplemented with 10 ng/mL FGF2 (Peprotech) and 10 ng/mL Human EGF
426 (Peprotech) and replated every 6-8 days. For astrocyte terminal differentiation,
427 expanded neural progenitors were re-plated at a density of 3×10^4 cells/cm² in
428 expansion media and 24 hours later switched to N2B27 supplemented with 10 ng/mL
429 human recombinant CNTF (Peprotech) and 10 ng/mL human recombinant BMP4
430 (Peprotech) for 7 days followed by media containing CNTF alone for another 13 days.
431 10 μ M Y-27632 was used for 24 hours before and after each replating. The protocol

432 for generating non-patterned astrocytes was the same as for floor plate-derived
433 astrocyte except the neural progenitors were derived with duo-SMAD inhibitors only
434 without ventral patterning reagents.

435 **Flow cytometry analysis and cell isolation**

436 Cells were dissociated in Accutase as described above and washed twice with DPBS
437 by centrifugation for 5 minutes at 200 rcf. For evaluating BFP expression, dissociated
438 cells were resuspended in 0.5 mM EDTA in DPBS (Sigma-Aldrich) and analysed on a
439 BD LSRFortessa cell analyser (BD Biosciences). For purifying BFP⁺ cells, dissociated
440 cells were resuspended in the same cell culture media. Background autofluorescence
441 was compensated for using KOLF2 parental cell line at a similar stage of differentiation
442 to define BFP⁻ gating. For purifying CD49f⁺ astrocytes, dissociated cells were stained
443 with Alexa Fluor 647-conjugated rat anti-CD49f antibody (5% v/v in a 100 µL reaction;
444 BD Biosciences) for 25 minutes at 37°C on an orbital shaker at 200 rcf and
445 resuspended in DPBS containing 0.5% bovine serum albumin and 50 units/mL DNase
446 I (Sigma Aldrich). Background autofluorescence was compensated for using KOLF2
447 parental cell line at a similar stage of differentiation to define BFP⁻ gating and unstained
448 astrocytes to define CD49f⁻ gating. Cell sorting was performed on a BD FACSAria III
449 (BD Biosciences) using an 80 µm nozzle. Sorted cells were collected in the same
450 media as for resuspension. Flow cytometry data were analysed in FlowJo v10.8.1 (BD
451 Biosciences) as shown in Figure S1B-E. Briefly, non-debris events were selected
452 using the eclipse gates on dot graphs of SSC-A versus FSC-A. Singlet events were
453 sequentially gated using polygonal gates on dot graphs of FSC-H versus FSC-A and
454 SSC-H versus SSC-A by selecting the events in the diagonal region. The positive and
455 negative gates in the fluorescence channel were set as bifurcate gates at a minimum
456 of 99.9% percentile (usually at 99.99% percentile) on the histogram of the
457 fluorescence intensity of the negative control sample of the same flow cytometry
458 experiment and applied to all samples of the same flow cytometry experiment.

459 **Immunocytochemistry**

460 Cultures were fixed with 3.7% PFA for 15-20 min at 4 °C. For nuclear antigen
461 detection, an additional fixation with methanol gradient was performed, which include

462 5 mins each in 33% and 66% methanol at room temperature followed by 100%
463 methanol for 20 min at -20°C. Cultures were then returned to PBST via inverse
464 gradient and were then permeabilized with three 10-minute washes in 0.3% Triton-X-
465 100 in PBS (PBS-T) and then blocked in PBS-T containing 1% BSA and 3% donkey
466 serum. Cells were incubated with primary antibodies in blocking solution overnight at
467 4°C. Following three PBS-T washes, Alexa-Fluor secondary antibodies (Thermo
468 Fisher Scientific) were added at 1:1000 PBS-T for 1 hour at ambient temperature in
469 the dark. Three PBS-T washes were then performed that included once with DAPI
470 (Molecular Probes). Images were taken on a Leica DMI6000B inverted microscope.
471 Quantification was carried out in Cell Profiler (Stirling et al. 2021) or manually using
472 ImageJ (Schindelin et al. 2012) by examining at least four randomly selected fields
473 from three independent experiments. The antibodies used are provided in the
474 Supplementary Table 1. Representative images shown in main figures were cropped
475 by randomly selecting the region of interest in the DAPI-stained channel only, with the
476 original unedited images shown in Figure S1A, S2 and S3.

477 **Single-cell RNA-sequencing**

478 Cells were dissociated with Accutase with 10 units/mL of papain (Sigma-Aldrich) for
479 10 minutes at 37°C and resuspended in 0.5% bovine serum albumin (Sigma Aldrich)
480 with 50 units/mL DNase I in DPBS without calcium or magnesium (Gibco) and passed
481 through a cell strainer with 35 µm mesh. Cells were stained with 1 µM SYTO16
482 (Invitrogen) and 0.08% (v/v) propidium iodide (part of the Invitrogen ReadyProbes™
483 Cell Viability Imaging Kit, Blue/Red) for 20 minutes on ice and then dispensed into the
484 nano-well plates of the ICELL8® cx Single-Cell System (Takara). Wells containing
485 single viable cells were automatically selected using the ICELL8 cx CellSelect v2.5
486 Software (Takara) with the green and not red logic. Manual triage was performed to
487 recover additional candidate wells that contain viable single cells. The library for
488 sequencing was then prepared using the SMART-Seq ICELL8 application kit (Takara)
489 following the manufacturer's recommended protocol. Next-generation sequencing was
490 performed using the NovaSeq6000 and the Xp Workflow on a S4 flow cell for 200
491 cycles of pair-end sequencing.

492 **Single-cell RNA-sequencing analysis**

493 Using the Cogent NGS Analysis Pipeline software v 1.5.1 (Takara), FASTQ files
494 containing all indices for each chip were demultiplexed to FASTQ files containing one
495 index per file. Adaptor sequences were removed using cutadapt 3.2 with the following
496 settings: -m 15 --trim-n --max-n 0.7 -q 20. Trimmed FASTQ files were aligned to the
497 *Homo sapiens* GRCh38.106 primary assembly with the BFP reporter gene attached
498 to the end of the genome, using STAR 2.7.9a (Dobin et al. 2013) with the following
499 settings: --outSAMtype BAM Unsorted --quantMode TranscriptomeSAM --
500 outReadsUnmapped Fastx --outSAMstrandField intronMotif --chimSegmentMin 12 --
501 chimJunctionOverhangMin 8 --chimOutJunctionFormat 1 --alignSJDBoverhangMin 10
502 --alignMatesGapMax 100000 --alignIntronMax 100000 --alignSJstitchMismatchNmax
503 5 -1 5 5 --chimMultimapScoreRange 3 --chimScoreJunctionNonGTAG -4 --
504 chimMultimapNmax 20 --chimNonchimScoreDropMin 10 --peOverlapNbasesMin 12 -
505 -peOverlapMMp 0.1 --alignInsertionFlush Right --
506 alignSplicedMateMapLminOverLmate 0 --alignSplicedMateMapLmin 30. After
507 alignment, gene-level quantification was performed using featureCounts from subread
508 2.0.0 (Liao et al. 2013) with the following settings: -t exon --primary -R CORE -F GTF
509 -Q 0 -B -g gene_id. The count matrix of each index was combined in R 4.2.0 (Team
510 2023).

511 All downstream analysis was performed in R 4.3.0 using Seurat 4.3.0 (Stuart et al.
512 2019). Gene-level filtering was applied by including only protein-coding genes with at
513 least five total counts across all cells and being expressed in at least 1% of all cells.
514 Poor quality cells were then identified using the *is.outlier* function from the scater
515 1.28.0 (McCarthy et al. 2017). Poor quality cells were defined as having a high
516 percentage of mitochondrial gene count, or high or low the total number of genes
517 detected, or high total gene counts. The thresholds of each metrics for each sample
518 were determined as twice the median absolute deviation of the sample. Raw gene
519 counts were log normalised with a scale.factor setting of 1×10^5 . Data from the two
520 batches of experiments were integrated using the *FindIntegrationAnchors* and
521 *IntegrateData* based on the common top 2000 highly variable genes and the first 30
522 dimensions of principal components. The percentage of mitochondrial gene count and

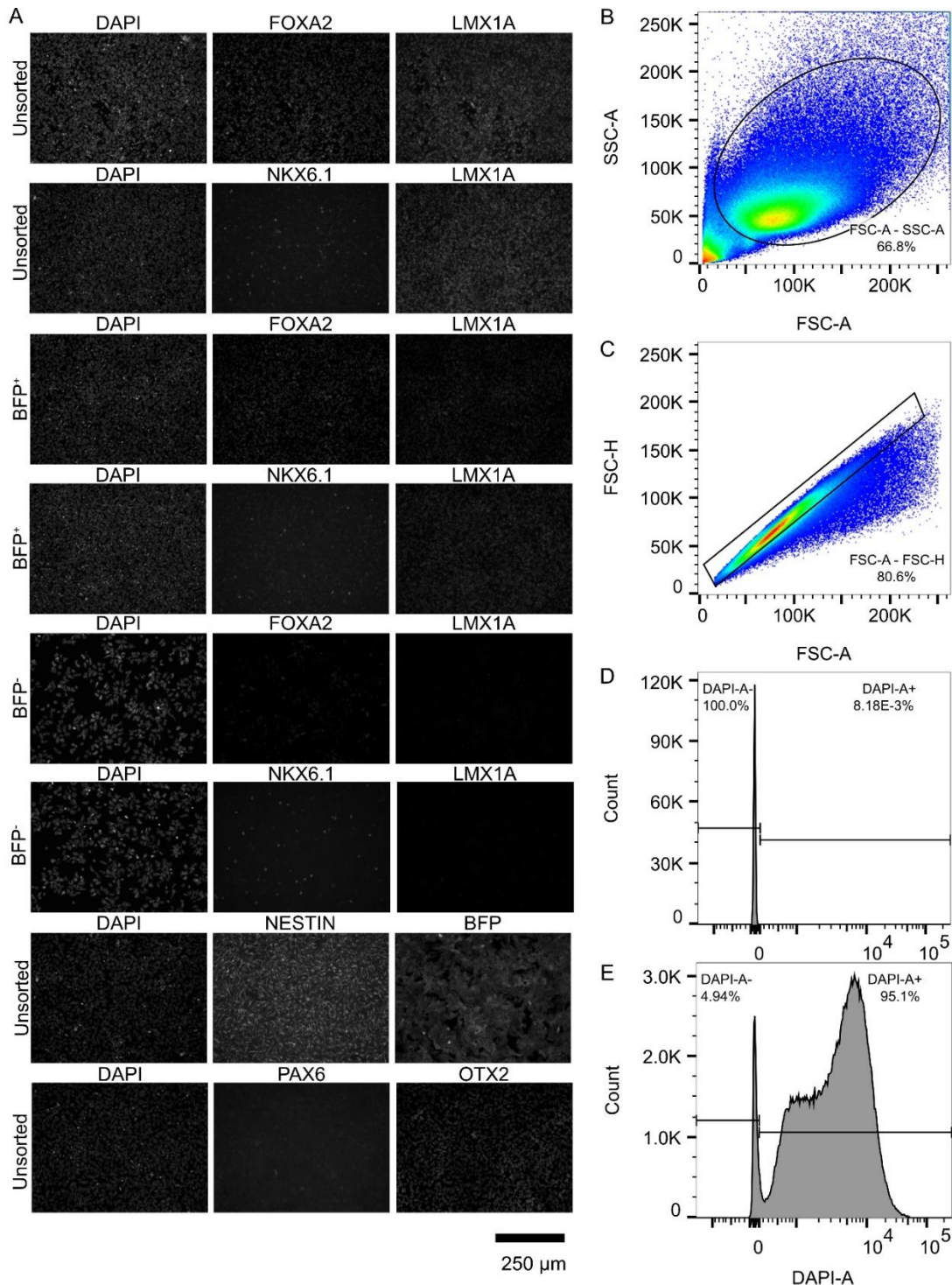
523 total gene count were regressed out using the *ScaleData* function. Principal
524 component analysis (PCA) was performed on the top 2000 high variable genes and
525 the number of principal components used for uniform manifold approximation and
526 projection (UMAP) was determined using the JackStraw method (Chung and Storey
527 2015). UMAP and unbiased Louvain clustering was performed on the first 33 principal
528 components. Pairwise differential gene expression analysis was performed using the
529 MAST method (Finak et al. 2015) with “Chip” as the latent variable. Gene ontology
530 enrichment analysis was performed using *enrichGO* function in the clusterProfiler
531 4.10.0 package (Stirling et al. 2021) with all genes in the filtered dataset as the
532 background. GO term database was downloaded using the org.Hs.eg.db 3.18.0
533 package (Carlson 2019). Revigo v1.8.1 was used to group the representative GO
534 terms based on semantic similarity using a size setting of 0.5, Homo sapiens
535 database, and SimRel method for semantic similarity (Schlicker et al. 2006; Supek et
536 al. 2011).

537 Published datasets were downloaded from NCBI’s Gene Expression Omnibus
538 (Clough and Barrett 2016) and processed in R 4.2.0. Gene level filtering was
539 performed by retaining only protein-coding genes with more than five total counts
540 across all cells. Gene counts were normalised using the *NormalizeData* function
541 (scale.factor settings are listed in Supplementary Table 2). PCA was performed based
542 on the top 2000 highly variable genes to obtain the first 50 PCs. Visual inspection of
543 the elbow plot was used to determine the number of PCs for downstream analysis.
544 Batch effect between subjects was evaluated on the two-dimensional PC2~PC1 plot.
545 Where inter-subject batch effect was observed, Harmony integration was performed
546 based on the PCs selected in the previous step (Supplementary Table 2). UMAP was
547 performed based on either the PCA or Harmony reduction (using the top 30
548 dimensions), and Louvain clustering was performed (settings shown in Supplementary
549 Table 2). Cluster identities were verified against the reported annotation where
550 possible. For datasets without detailed annotation published or astrocyte lineage
551 reported (Supplementary Table 2), reannotation was performed based on the
552 expression of known markers (Figure S7A-E). Reference mapping was performed
553 using *FindTransferAnchors* and *TransferData* function in Seurat based on the first 30
554 dimensions of either the PCA or Harmony loadings of the reference dataset.

555 **Statistical analyses**

556 All data were collected from at least three independent experiments and presented as
557 mean \pm standard error of means unless otherwise specified. Data were tested for
558 normality with the Shapiro-Wilk test and for equal variance with Levene test before
559 performing statistical analyses by two-way ANOVA with post-hoc Tukey test for
560 multiple comparisons where relevant. Kruskal-Wallis test with post-hoc Dunn's test for
561 pairwise comparison was used where parametric test was not suitable. Effect size was
562 calculated as Cohen's f for ANOVA or eta squared based on the H-statistic for Kruskal-
563 Wallis test. All statistical tests were performed in R4.3.0.

564 Supplementary Information



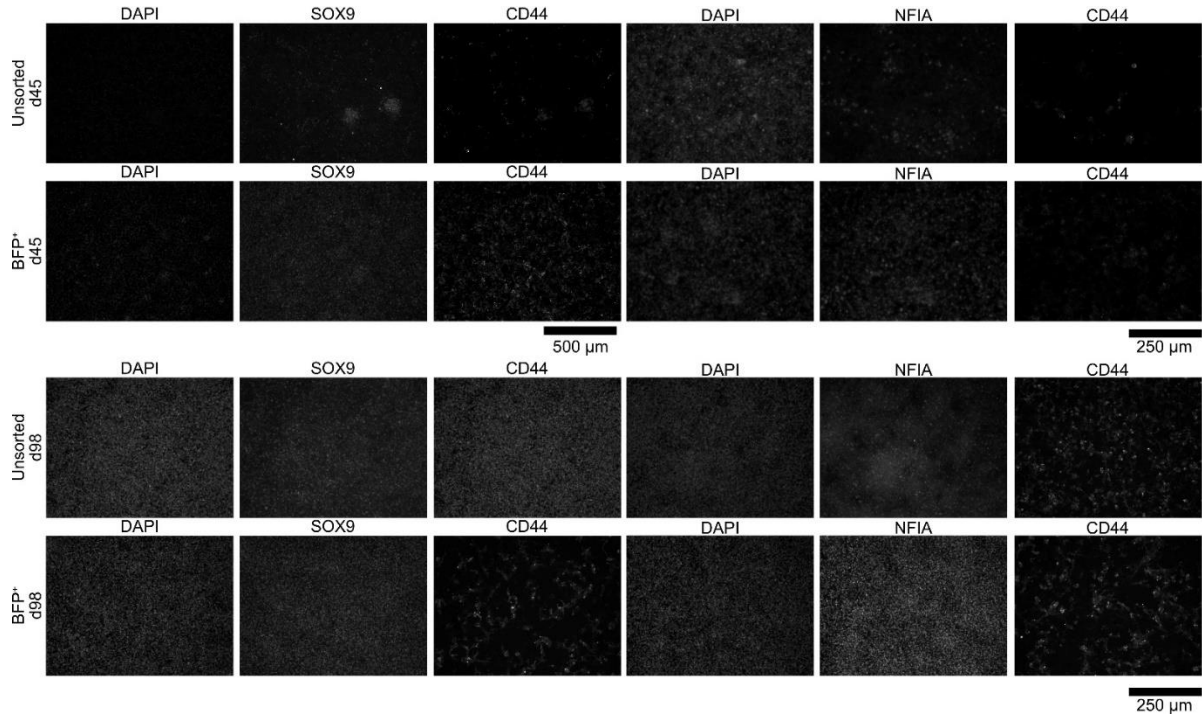
565

566 **Figure S1. Original images of immunocytochemistry of d19 progenitors and**
567 **gating strategy of BFP flow cytometry analysis.**

568 A, the original images shown in Figure 1B-C. The gating strategy used for BFP flow
569 cytometry analysis are shown in B-E and described in Methods and Materials. B,

570 scatter plot of SSC-A versus FSC-A. C, scatter plot of FSC-H versus FSC-A. D-E,
571 histogram of BFP fluorescence in the negative control (D) and BFP-expressing (E)
572 samples.

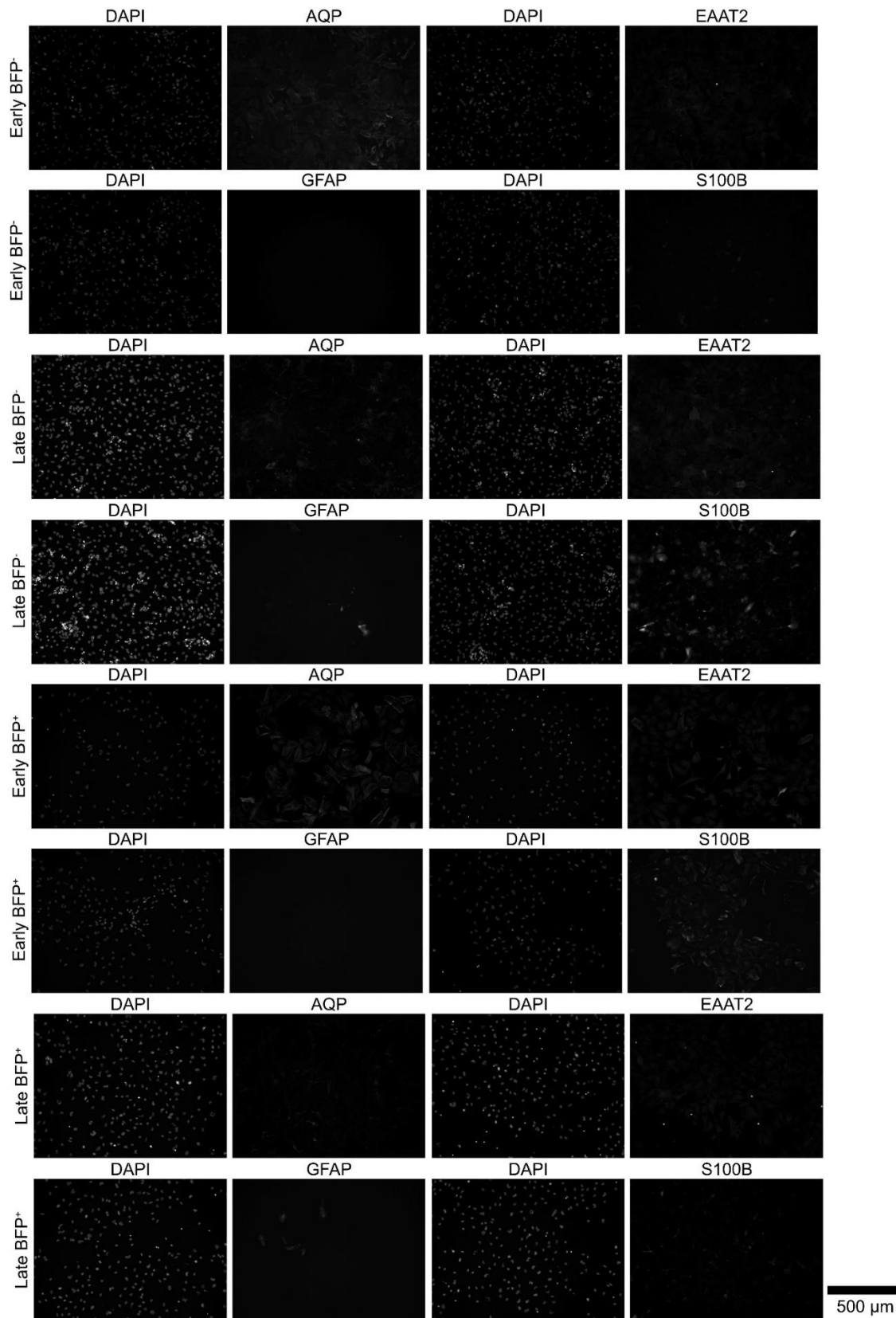
573



574

575 **Figure S2. Original images of immunocytochemistry of astrogenic markers**

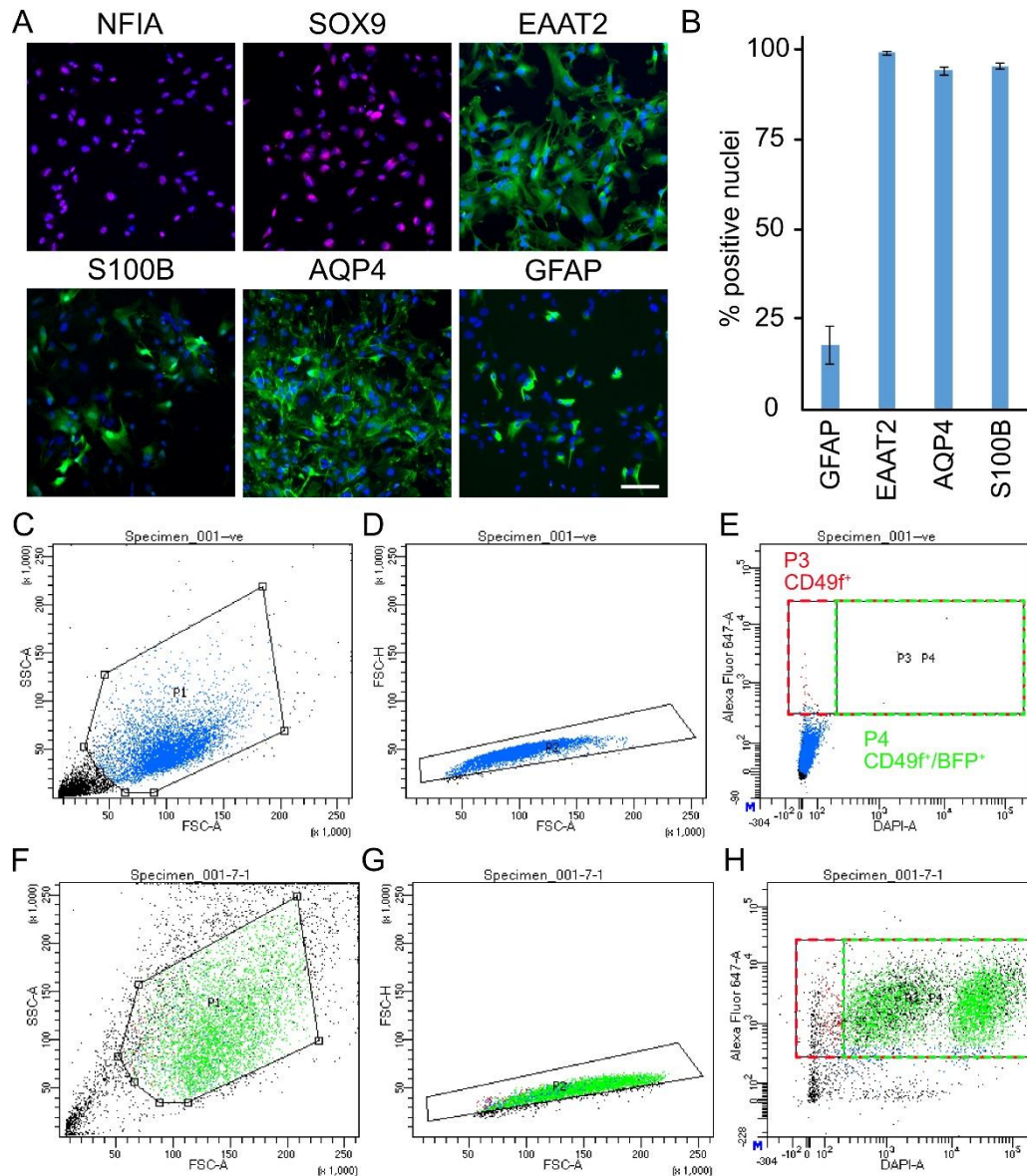
576 **shown in Figure 2A.**



577

578 **Figure S3. Original images of immunocytochemistry of astrocyte markers**

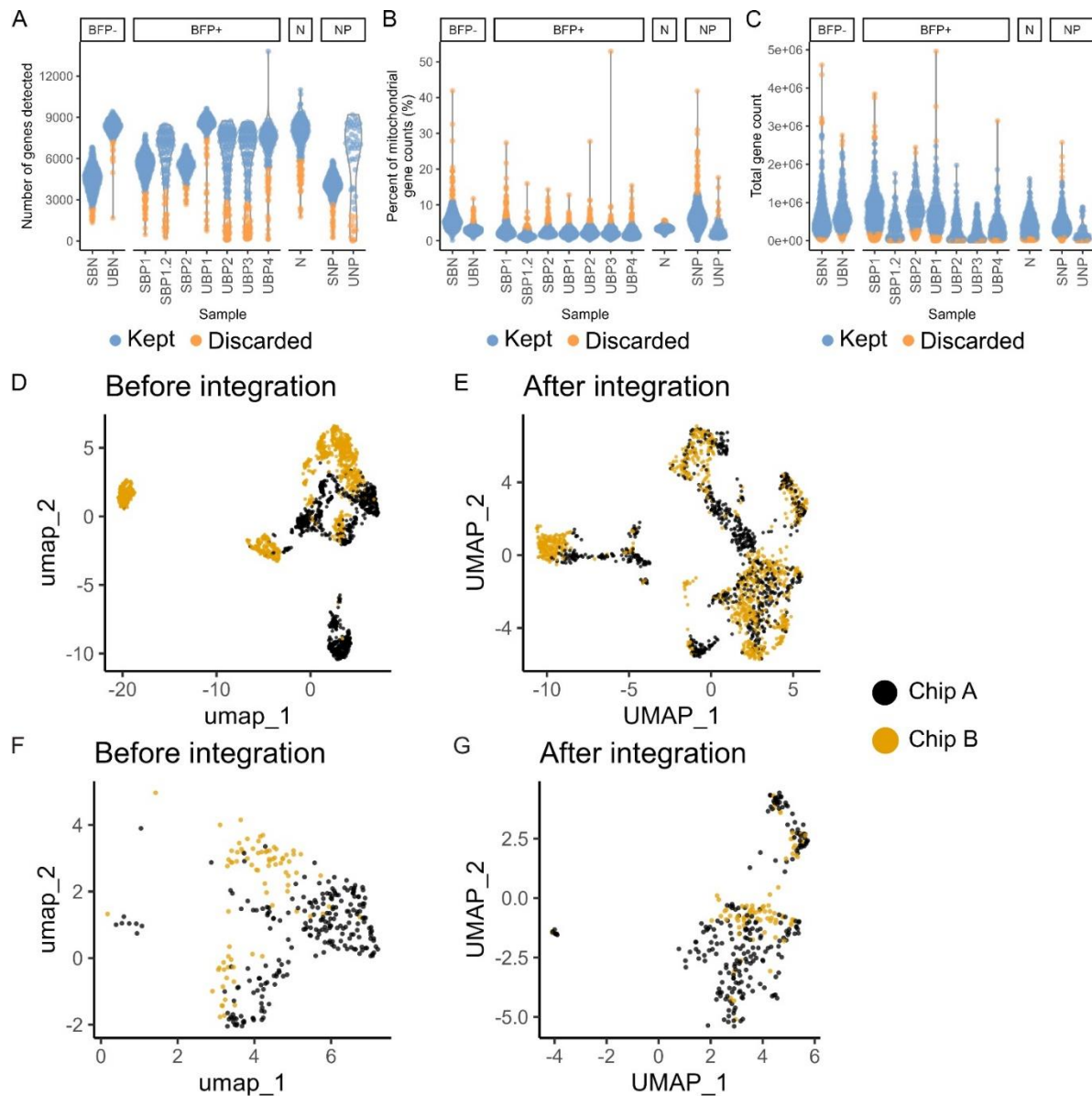
579 **shown in Figure 2B.**



580

581 **Figure S4. Non-patterned astrocytes and fluorescence-activated cell sorting of**
582 **astrocytes for single cell RNA sequencing.**

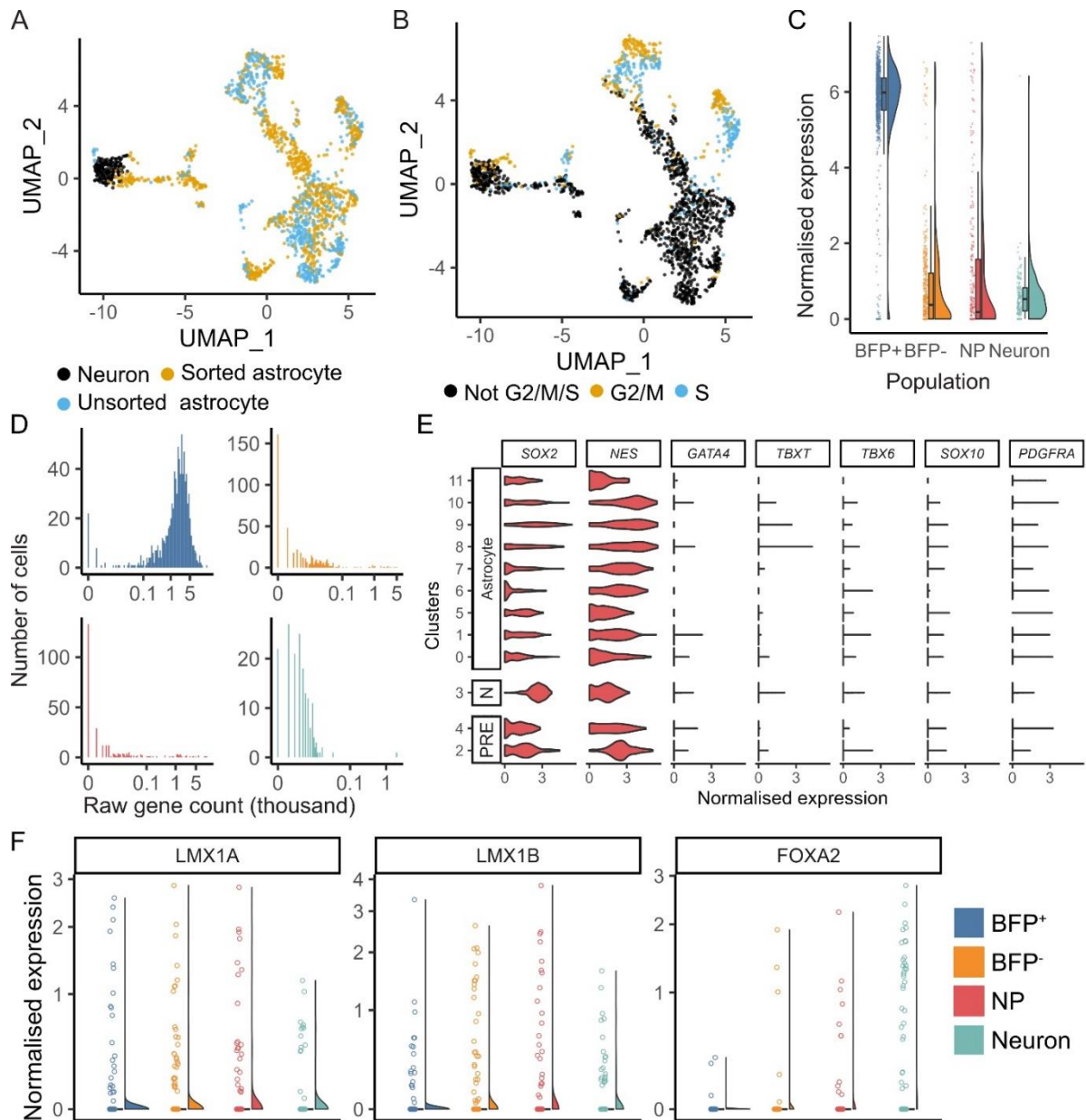
583 A, Representative view of immunocytochemistry of astrocyte marker expression in
584 non-patterned astrocytes (scale bar represents 100 μ m). B, Quantification of astrocyte
585 marker expression in astrocytes. Error bars represent SEM of three independent
586 experiments. C-E, negative control samples; F-H, one sample of BFP+ astrocytes). C
587 and F shows the dot plot of SSC-A versus FSC-A. D and G shows the dot plot of FSC-
588 H versus FSC-A. E and H shows the dot plot of Alexa Fluor-647-A (labelling CD49f)
589 versus DAPI-A (labelling BFP). P3 was used to isolate CD49f⁺ population (including
590 both BFP⁺ and BFP⁻), while P4 was used to isolate CD49f⁺/BFP⁺ population.



591

592 **Figure S5. Processing of single cell RNA sequencing data.**

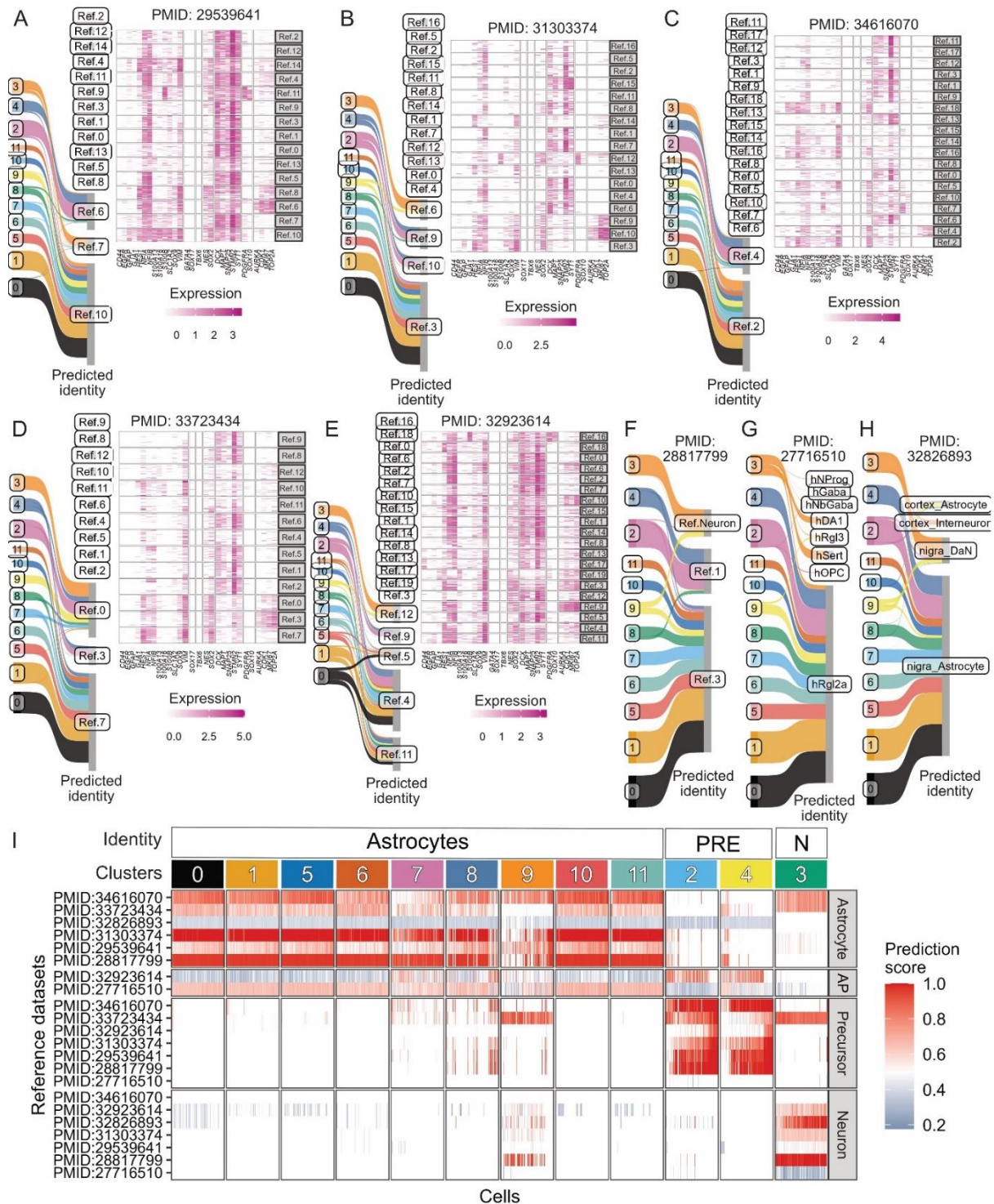
593 A-C, Violin plots showing the results of adaptive cell-level filtering based on the
594 number of genes detected per cell (A), percentage of mitochondrial gene counts per
595 cell (B), and total gene count per cell (C). D-E, UMAP plot of all filtered cells before
596 (D) and after integration (E) coloured by chip. F-G, UMAP plot of the subset of sorted
597 BFP+ astrocytes on Chip A and B derived from the same astrocyte differentiation
598 before (F) and after integration (G) coloured by chip. (N: neuron; SBN: sorted BFP-;
599 SBP: sorted BFP+; SNP: sorted non-patterned; UBN: unsorted BFP-; UBP: unsorted
600 BFP+; UNP: unsorted non-patterned; numbers represent independent samples)



601

602 **Figure S6. Marker expression in scRNAseq.**

603 A-B, UMAP plot of all filtered cells after integration coloured by sample type and sorting
 604 status (A) and estimated cell cycle phase (B). C, Raincloud plots of normalised
 605 expression of *BFP*. D, Histogram of the distribution of raw gene count of *BFP*. E, Violin
 606 plots of the normalised expression of endoderm, mesoderm, neuroectoderm, and
 607 oligodendrocyte progenitor markers. F, Violin plots of the normalised expression of
 608 classic ventral midbrain markers.



609

610 **Figure S7. Reference mapping to human brain single cell RNA sequencing**

611 **datasets.**

612 A-H, Sankey plot summarising the result of reference mapping of cells in different

613 clusters to eight published reference human brain scRNAseq datasets. The thickness

614 of the thread is proportional to the number of cells mapped to the same identity in the

615 reference datasets (predicted identity). Cluster IDs in this study are shown on the left.
 616 Heatmap in Panel A-E shows the expression of marker genes in different clusters in
 617 the re-annotated reference datasets. I, Heatmap of prediction score from Seurat
 618 integration.

619

620 **Supplementary Table 1. Antibodies used in this study.**

Target	Species	Producer	Catalogue number	Dilution for use
ALDH1L1	MS	Abcam	ab56777	1:500
AQP4	RB	Abcam	ab259318	1:200
BFP	rabbit	Evrogen	AB233	1:3000
CD44	mouse	Cell Signalling Technology	3750	1:400
EAAT2	goat	Abcam	ab235202	1:200
FOXA2	goat	R&D system	AF2400	1:1000
GFAP	rat	Life Tech	AB10533	1:1000
LMX1A	rabbit	Millipore	HPA030088	1:2000
NESTIN	mouse	BD	BD611659	1:300
NFIA	rabbit	Abcam	AB228897	1:1000
NKX6.1	mouse	DSHB	F55A10	1:100
OTX2	goat	R&D system	AF1979	1:200
PAX6	mouse	DSHB	PAX6	1:1000
S100B	rabbit	Abcam	ab52642	1:1000
SOX9	goat	R&D system	AF3075	1:300
Anti-Goat IgG, Alexa Fluor 488	donkey	Invitrogen	A32814	1:1000
Anti-Goat IgG, Alexa Fluor 555	donkey	Invitrogen	A32816	1:1000
Anti-Goat IgG, Alexa Fluor 647	donkey	Invitrogen	A32849	1:1000

Anti-Mouse IgG, Alexa Fluor 488	donkey	Invitrogen	A21202	1:1000
Anti-Mouse IgG, Alexa Fluor 555	donkey	Invitrogen	A31570	1:1000
Anti-Mouse IgG, Alexa Fluor 647	donkey	Invitrogen	A31571	1:1000
Anti-Rabbit IgG, Alexa Fluor 488	donkey	Invitrogen	A21206	1:1000
Anti-Rabbit IgG, Alexa Fluor 555	donkey	Invitrogen	A31572	1:1000
Anti-Rabbit IgG, Alexa Fluor 647	donkey	Invitrogen	A31573	1:1000
Anti-Rat IgG, Alexa Fluor 488	donkey	Invitrogen	A21208	1:1000

621

622 **Supplementary Table 2. Settings used for processing published datasets.**

PMID	Tissue	Age	Scale factor	PCs used	Harmony integration	Clustering resolution	Re-annotation
3282 6893	SN and cortex	Adult	10000	50	No	0.5	No
3372 3434	multiple	CS22	10000	50	Yes	0.3	Yes
3461 6070	multiple	GW25	10000	50	Yes	0.4	Yes
3292 3614	Neocortex	GW9-28	100000	30	Yes	0.9	Yes
3130 3374	Neocortex	GW17-18	10000	30	Yes	0.5	Yes
2953 9641	Prefrontal cortex	GW8-26	100000	30	Yes	0.9	Yes
2881 7799	PSC-derived astrocytes	-	10000	30	No	0.3	No
2771 6510	Ventral midbrain	GW7-11	10000	30	No	0.5	No

623

624 Supplementary Data 1: Pairwise DEGs of three astrocyte and one neuron populations.

625 Supplementary Data 2: GO enrichment of population enriched DEGs.

626 Supplementary Data 3: Representative enriched GO terms of DEGs for BFP+ and
627 BFP- astrocytes.

628 Supplementary Data 4: DEGs comparing sorted and unsorted populations.

629 **Acknowledgements**

630 We would like to thank Mark Bishop and Joanne Morgan for conducting FACS and
631 next generation sequencing, respectively. We thank Kathryn Peall and Laura Abram
632 for providing iPSC-derived neurons for scRNAseq. We also thank the support of the
633 Supercomputing Wales project, which is part-funded by the European Regional
634 Development Fund (ERDF) via the Welsh Government.

635 **Author Contribution**

636 Z.L. and M.L. conceived the study and designed the experiments. Z.L. performed all
637 cell experiments and analysed all data. L.C. and M.L. designed the lineage tracing
638 system, and L.C. generated the cell line with assistance from Z.L. M.R. performed
639 iCELL8 library preparation. J.M.S., F.W., and V.V. provided guidance and contributed
640 to general discussions on scRNAseq data analysis. C.W. contributed to the design of
641 scRNAseq and general discussions throughout the work. Z.L. and M.L. wrote the
642 paper. All authors edited and approved the paper.

643 **Funding**

644 This work was supported by the UK Dementia Research Institute, jointly funded by the
645 UK Medical Research Council, Alzheimer's Society and Alzheimer's Research UK, to
646 C.W. (MC_PC_17112) and Z.L. (DRI-TRA2021-02), and a seed corn fund to Z.L. from
647 the Neuroscience and Mental Health Innovation Institute, Cardiff University. Z.L. was
648 funded by a UK Dementia Research Institute PhD studentship.

649 **Data Availability**

650 The sequencing data discussed in this publication have been deposited in NCBI's
651 Gene Expression Omnibus (Clough and Barrett 2016) and are accessible through a
652 GEO Series accession number which will be made available upon final publication.

653 **Declaration of interests**

654 The authors declare no competing interests.

655 **References**

656 Agarwal, D. et al. 2020. A single-cell atlas of the human substantia nigra reveals cell-
657 specific pathways associated with neurological disorders. *Nat Commun* 11(1), p. 4183.
658 doi: 10.1038/s41467-020-17876-0

659

660 Ahmed, M., Owens, M. J. S., Toledo, E. M., Arenas, E., Bradley, M. and Ffrench-
661 Constant, C. 2021. Combinatorial ECM Arrays Identify Cooperative Roles for
662 Matricellular Proteins in Enhancing the Generation of TH+ Neurons From Human
663 Pluripotent Cells. *Front Cell Dev Biol* 9, p. 755406. doi: 10.3389/fcell.2021.755406

664

665 Andersson, E. et al. 2006. Identification of intrinsic determinants of midbrain dopamine
666 neurons. *Cell* 124(2), pp. 393-405. doi: 10.1016/j.cell.2005.10.037

667

668 Barbar, L. et al. 2020. CD49f Is a Novel Marker of Functional and Reactive Human
669 iPSC-Derived Astrocytes. *Neuron* 107(3), pp. 436-453 e412. doi:
670 10.1016/j.neuron.2020.05.014

671

672 Barbuti, P. A. et al. 2020. iPSC-derived midbrain astrocytes from Parkinson's disease
673 patients carrying pathogenic SNCA mutations exhibit alpha-synuclein aggregation,
674 mitochondrial fragmentation and excess calcium release. *bioRxiv*, p.
675 2020.2004.2027.053470. doi: 10.1101/2020.04.27.053470

676

- 677 Batiuk, M. Y. et al. 2020. Identification of region-specific astrocyte subtypes at single
678 cell resolution. *Nature Communications* 11(1), doi: 10.1038/s41467-019-14198-8
679
- 680 Bayraktar, O. A. et al. 2020. Astrocyte layers in the mammalian cerebral cortex
681 revealed by a single-cell in situ transcriptomic map. *Nature Neuroscience* 23(4), pp.
682 500-509. doi: 10.1038/s41593-020-0602-1
683
- 684 Bhaduri, A. et al. 2021. An atlas of cortical arealization identifies dynamic molecular
685 signatures. *Nature* 598(7879), pp. 200-204. doi: 10.1038/s41586-021-03910-8
686
- 687 Bifsha, P., Balsalobre, A. and Drouin, J. 2017. Specificity of Pitx3-Dependent Gene
688 Regulatory Networks in Subsets of Midbrain Dopamine Neurons. *Molecular*
689 *Neurobiology* 54(7), pp. 4921-4935. doi: 10.1007/s12035-016-0040-y
690
- 691 Booth, H. D. E., Hirst, W. D. and Wade-Martins, R. 2017. The Role of Astrocyte
692 Dysfunction in Parkinson's Disease Pathogenesis. *Trends in neurosciences* 40(6), pp.
693 358-370. doi: 10.1016/j.tins.2017.04.001
694
- 695 Booth, H. D. E. et al. 2019. RNA sequencing reveals MMP2 and TGFB1
696 downregulation in LRRK2 G2019S Parkinson's iPSC-derived astrocytes. *Neurobiol*
697 *Dis* 129, pp. 56-66. doi: 10.1016/j.nbd.2019.05.006
698
- 699 Bradley, R. A. et al. 2019. Regionally specified human pluripotent stem cell-derived
700 astrocytes exhibit different molecular signatures and functional properties.
701 *Development* 146(13), p. dev170910. doi: 10.1242/dev.170910
702
- 703 Cardo, L. F., Monzón-Sandoval, J., Li, Z., Webber, C. and Li, M. 2023. Single-Cell
704 Transcriptomics and In Vitro Lineage Tracing Reveals Differential Susceptibility of
705 Human iPSC-Derived Midbrain Dopaminergic Neurons in a Cellular Model of
706 Parkinson's Disease. *Cells* 12(24), doi: 10.3390/cells12242860
707
- 708 Carlson, M. 2019. org.Hs.eg.db: Genome wide annotation for Human. R package
709 version 3.8.2.
710

- 711 Chai, H. et al. 2017. Neural Circuit-Specialized Astrocytes: Transcriptomic, Proteomic,
712 Morphological, and Functional Evidence. *Neuron* 95(3), pp. 531-549 e539. doi:
713 10.1016/j.neuron.2017.06.029
- 714
- 715 Chandrasekaran, A., Avci, H. X., Leist, M., Kobilák, J. and Dinnyés, A. 2016.
716 Astrocyte Differentiation of Human Pluripotent Stem Cells: New Tools for Neurological
717 Disorder Research. *Frontiers in cellular neuroscience* 10, pp. 215-215. doi:
718 10.3389/fncel.2016.00215
- 719
- 720 Chung, N. C. and Storey, J. D. 2015. Statistical significance of variables driving
721 systematic variation in high-dimensional data. *Bioinformatics* 31(4), pp. 545-554. doi:
722 10.1093/bioinformatics/btu674
- 723
- 724 Clough, E. and Barrett, T. 2016. The Gene Expression Omnibus Database. *Methods*
725 *Mol Biol* 1418, pp. 93-110. doi: 10.1007/978-1-4939-3578-9_5
- 726
- 727 Crompton, L. A., McComish, S. F., Stathakos, P., Cordero-Llana, O., Lane, J. D. and
728 Caldwell, M. A. 2021. Efficient and Scalable Generation of Human Ventral Midbrain
729 Astrocytes from Human-Induced Pluripotent Stem Cells. *Journal of Visualized*
730 *Experiments* (176), doi: 10.3791/62095
- 731
- 732 Crompton, L. A., McComish, S. F., Steward, T. G. J., Whitcomb, D. J., Lane, J. D. and
733 Caldwell, M. A. 2023. Human stem cell-derived ventral midbrain astrocytes exhibit a
734 region-specific secretory profile. *Brain Commun* 5(2), p. fcad114. doi:
735 10.1093/braincomms/fcad114
- 736
- 737 de Rus Jacquet, A., Tancredi, J. L., Lemire, A. L., DeSantis, M. C., Li, W. P. and
738 O'Shea, E. K. 2021. The LRRK2 G2019S mutation alters astrocyte-to-neuron
739 communication via extracellular vesicles and induces neuron atrophy in a human
740 iPSC-derived model of Parkinson's disease. *Elife* 10, p. 2020.2007.2002.178574. doi:
741 10.7554/eLife.73062
- 742
- 743 Deneen, B., Ho, R., Lukaszewicz, A., Hochstim, C. J., Gronostajski, R. M. and
744 Anderson, D. J. 2006. The Transcription Factor NFIA Controls the Onset of
745 Gliogenesis in the Developing Spinal Cord. *Neuron* 52(6), pp. 953-968. doi:
746 10.1016/j.neuron.2006.11.019

747

748 di Domenico, A. et al. 2019. Patient-Specific iPSC-Derived Astrocytes Contribute to
749 Non-Cell-Autonomous Neurodegeneration in Parkinson's Disease. *Stem cell reports*
750 12(2), pp. 213-229. doi: 10.1016/j.stemcr.2018.12.011

751

752 Dobin, A. et al. 2013. STAR: ultrafast universal RNA-seq aligner. *Bioinformatics* 29(1),
753 pp. 15-21. doi: 10.1093/bioinformatics/bts635

754

755 Duan, D., Fu, Y., Paxinos, G. and Watson, C. 2013. Spatiotemporal expression
756 patterns of Pax6 in the brain of embryonic, newborn, and adult mice. *Brain Structure*
757 *and Function* 218(2), pp. 353-372. doi: 10.1007/s00429-012-0397-2

758

759 Endo, F. et al. 2022. Molecular basis of astrocyte diversity and morphology across the
760 CNS in health and disease. *Science* 378(6619), p. eadc9020. doi:
761 doi:10.1126/science.adc9020

762

763 Eze, U. C., Bhaduri, A., Haeussler, M., Nowakowski, T. J. and Kriegstein, A. R. 2021.
764 Single-cell atlas of early human brain development highlights heterogeneity of human
765 neuroepithelial cells and early radial glia. *Nature Neuroscience* 24(4), pp. 584-594.
766 doi: 10.1038/s41593-020-00794-1

767

768 Falk, A. et al. 2012. Capture of neuroepithelial-like stem cells from pluripotent stem
769 cells provides a versatile system for in vitro production of human neurons. *PLOS ONE*
770 7(1), p. e29597. doi: 10.1371/journal.pone.0029597

771

772 Fan, X. et al. 2020. Single-cell transcriptome analysis reveals cell lineage specification
773 in temporal-spatial patterns in human cortical development. *Science Advances* 6(34),
774 p. eaaz2978. doi: doi:10.1126/sciadv.aaz2978

775

776 Finak, G. et al. 2015. MAST: a flexible statistical framework for assessing
777 transcriptional changes and characterizing heterogeneity in single-cell RNA
778 sequencing data. *Genome Biology* 16(1), p. 278. doi: 10.1186/s13059-015-0844-5

779

780 Gabay, L., Lowell, S., Rubin, L. L. and Anderson, D. J. 2003. Deregulation of
781 dorsoventral patterning by FGF confers trilineage differentiation capacity on CNS stem
782 cells in vitro. *Neuron* 40(3), pp. 485-499. doi: 10.1016/s0896-6273(03)00637-8

783

784 Hedegaard, A., Monzón-Sandoval, J., Newey, S. E., Whiteley, E. S., Webber, C. and
785 Akerman, C. J. 2020. Pro-maturational Effects of Human iPSC-Derived Cortical
786 Astrocytes upon iPSC-Derived Cortical Neurons. *Stem cell reports* 15(1), pp. 38-51.
787 doi: <https://doi.org/10.1016/j.stemcr.2020.05.003>

788

789 Holmqvist, S. et al. 2015. Generation of human pluripotent stem cell reporter lines for
790 the isolation of and reporting on astrocytes generated from ventral midbrain and
791 ventral spinal cord neural progenitors. *Stem Cell Research* 15(1), pp. 203-220. doi:
792 <https://doi.org/10.1016/j.scr.2015.05.014>

793

794 Houweling, A. C., Dildrop, R., Peters, T., Mummenhoff, J., Moorman, A. F. M., Rütger,
795 U. and Christoffels, V. M. 2001. Gene and cluster-specific expression of the Iroquois
796 family members during mouse development. *Mechanisms of Development* 107(1), pp.
797 169-174. doi: [https://doi.org/10.1016/S0925-4773\(01\)00451-8](https://doi.org/10.1016/S0925-4773(01)00451-8)

798

799 Itoh, N. et al. 2018. Cell-specific and region-specific transcriptomics in the multiple
800 sclerosis model: Focus on astrocytes. *Proceedings of the National Academy of
801 Sciences* 115(2), pp. E302-E309. doi: doi:10.1073/pnas.1716032115

802

803 Jaeger, I. et al. 2011. Temporally controlled modulation of FGF/ERK signaling directs
804 midbrain dopaminergic neural progenitor fate in mouse and human pluripotent stem
805 cells. *Development* 138(20), pp. 4363-4374. doi: 10.1242/dev.066746

806

807 Jain, M., Armstrong, R. J., Tyers, P., Barker, R. A. and Rosser, A. E. 2003. GABAergic
808 immunoreactivity is predominant in neurons derived from expanded human neural
809 precursor cells in vitro. *Exp Neurol* 182(1), pp. 113-123. doi: 10.1016/s0014-
810 4886(03)00055-4

811

812 Kamath, T. et al. 2022. Single-cell genomic profiling of human dopamine neurons
813 identifies a population that selectively degenerates in Parkinson's disease. *Nature
814 Neuroscience* 25(5), pp. 588-595. doi: 10.1038/s41593-022-01061-1

815

816 Koch, P., Opitz, T., Steinbeck, J. A., Ladewig, J. and Brüstle, O. 2009. A rosette-type,
817 self-renewing human ES cell-derived neural stem cell with potential for in vitro
818 instruction and synaptic integration. *Proc Natl Acad Sci U S A* 106(9), pp. 3225-3230.
819 doi: 10.1073/pnas.0808387106

820

821 Kostuk, E. W., Cai, J. and Iacovitti, L. 2019. Subregional differences in astrocytes
822 underlie selective neurodegeneration or protection in Parkinson's disease models in
823 culture. *Glia* 67(8), pp. 1542-1557. doi: 10.1002/glia.23627

824

825 Krencik, R., Weick, J. P., Liu, Y., Zhang, Z.-J. and Zhang, S.-C. 2011. Specification of
826 transplantable astroglial subtypes from human pluripotent stem cells. *Nature*
827 *Biotechnology* 29, p. 528. doi: 10.1038/nbt.1877

828 <https://www.nature.com/articles/nbt.1877#supplementary-information>

829

830 La Manno, G. et al. 2016. Molecular Diversity of Midbrain Development in Mouse,
831 Human, and Stem Cells. *Cell* 167(2), pp. 566-580.e519. doi:
832 10.1016/j.cell.2016.09.027

833

834 Li, Y. et al. 2023. Spatiotemporal transcriptome atlas reveals the regional specification
835 of the developing human brain. *Cell* 186(26), pp. 5892-5909.e5822. doi:
836 <https://doi.org/10.1016/j.cell.2023.11.016>

837

838 Liao, Y., Smyth, G. K. and Shi, W. 2013. The Subread aligner: fast, accurate and
839 scalable read mapping by seed-and-vote. *Nucleic Acids Res* 41(10), p. e108. doi:
840 10.1093/nar/gkt214

841

842 Lin, Y.-T. et al. 2018. APOE4 Causes Widespread Molecular and Cellular Alterations
843 Associated with Alzheimer's Disease Phenotypes in Human iPSC-Derived Brain Cell
844 Types. *Neuron* 98(6), pp. 1141-1154.e1147. doi:
845 <https://doi.org/10.1016/j.neuron.2018.05.008>

846

847 Liu, Y. et al. 2004. CD44 expression identifies astrocyte-restricted precursor cells.
848 *Developmental Biology* 276(1), pp. 31-46. doi:
849 <https://doi.org/10.1016/j.ydbio.2004.08.018>

850

- 851 Lozzi, B., Huang, T. W., Sardar, D., Huang, A. Y. S. and Deneen, B. 2020. Regionally
852 Distinct Astrocytes Display Unique Transcription Factor Profiles in the Adult Brain.
853 *Frontiers in Neuroscience* 14, doi: 10.3389/fnins.2020.00061
- 854
- 855 Makarava, N., Chang, J. C.-Y., Kushwaha, R. and Baskakov, I. V. 2019. Region-
856 Specific Response of Astrocytes to Prion Infection. *Frontiers in Neuroscience* 13, doi:
857 10.3389/fnins.2019.01048
- 858
- 859 Matsunaga, E., Araki, I. and Nakamura, H. 2001. Role of Pax3/7 in the tectum
860 regionalization. *Development* 128(20), pp. 4069-4077. doi: 10.1242/dev.128.20.4069
- 861
- 862 McCarthy, D. J., Campbell, K. R., Lun, A. T. L. and Wills, Q. F. 2017. Scater: pre-
863 processing, quality control, normalization and visualization of single-cell RNA-seq data
864 in R. *Bioinformatics* 33(8), pp. 1179-1186. doi: 10.1093/bioinformatics/btw777
- 865
- 866 Molofsky, A. V. et al. 2012. Astrocytes and disease: a neurodevelopmental
867 perspective. *Genes & Development* 26(9), pp. 891-907. doi: 10.1101/gad.188326.112
- 868
- 869 Morel, L. et al. 2017. Molecular and Functional Properties of Regional Astrocytes in
870 the Adult Brain. *J Neurosci* 37(36), pp. 8706-8717. doi: 10.1523/JNEUROSCI.3956-
871 16.2017
- 872
- 873 Nolbrant, S., Heuer, A., Parmar, M. and Kirkeby, A. 2017. Generation of high-purity
874 human ventral midbrain dopaminergic progenitors for in vitro maturation and
875 intracerebral transplantation. *Nature Protocols* 12(9), pp. 1962-1979. doi:
876 10.1038/nprot.2017.078
- 877
- 878 Oberheim, N. A. et al. 2009. Uniquely hominid features of adult human astrocytes. *J*
879 *Neurosci* 29(10), pp. 3276-3287. doi: 10.1523/jneurosci.4707-08.2009
- 880
- 881 Peteri, U.-K., Pitkonen, J., Utami, K. H., Paavola, J., Roybon, L., Pouladi, M. A. and
882 Castrén, M. L. 2021. Generation of the Human Pluripotent Stem-Cell-Derived
883 Astrocyte Model with Forebrain Identity. *Brain sciences* 11(2), p. 209. doi:
884 10.3390/brainsci11020209

885

886 Phatnani, H. and Maniatis, T. 2015. Astrocytes in neurodegenerative disease. *Cold*
887 *Spring Harbor perspectives in biology* 7(6), p. a020628. doi:
888 10.1101/cshperspect.a020628

889

890 Polioudakis, D. et al. 2019. A Single-Cell Transcriptomic Atlas of Human Neocortical
891 Development during Mid-gestation. *Neuron* 103(5), pp. 785-801.e788. doi:
892 10.1016/j.neuron.2019.06.011

893

894 Roybon, L. et al. 2013. Human stem cell-derived spinal cord astrocytes with defined
895 mature or reactive phenotypes. *Cell Rep* 4(5), pp. 1035-1048. doi:
896 10.1016/j.celrep.2013.06.021

897

898 Schindelin, J. et al. 2012. Fiji: an open-source platform for biological-image analysis.
899 *Nature Methods* 9(7), pp. 676-682. doi: 10.1038/nmeth.2019

900

901 Schlicker, A., Domingues, F. S., Rahnenführer, J. and Lengauer, T. 2006. A new
902 measure for functional similarity of gene products based on Gene Ontology. *BMC*
903 *Bioinformatics* 7(1), p. 302. doi: 10.1186/1471-2105-7-302

904

905 Schober, A. L., Wicki-Stordeur, L. E., Murai, K. K. and Swayne, L. A. 2022.
906 Foundations and implications of astrocyte heterogeneity during brain development
907 and disease. *Trends in neurosciences* 45(9), pp. 692-703. doi:
908 10.1016/j.tins.2022.06.009

909

910 Serio, A. et al. 2013. Astrocyte pathology and the absence of non-cell autonomy in an
911 induced pluripotent stem cell model of TDP-43 proteinopathy. *Proceedings of the*
912 *National Academy of Sciences of the United States of America* 110(12), pp. 4697-
913 4702. doi: 10.1073/pnas.1300398110

914

915 Sloan, S. A. et al. 2017. Human Astrocyte Maturation Captured in 3D Cerebral Cortical
916 Spheroids Derived from Pluripotent Stem Cells. *Neuron* 95(4), pp. 779-790 e776. doi:
917 10.1016/j.neuron.2017.07.035

918

- 919 Sonninen, T.-M. et al. 2020. Metabolic alterations in Parkinson's disease astrocytes.
920 *Scientific Reports* 10(1), p. 14474. doi: 10.1038/s41598-020-71329-8
- 921
- 922 Stirling, D. R., Swain-Bowden, M. J., Lucas, A. M., Carpenter, A. E., Cimini, B. A. and
923 Goodman, A. 2021. CellProfiler 4: improvements in speed, utility and usability. *BMC*
924 *Bioinformatics* 22(1), p. 433. doi: 10.1186/s12859-021-04344-9
- 925
- 926 Stolt, C. C., Lommes, P., Sock, E., Chaboissier, M.-C., Schedl, A. and Wegner, M.
927 2003. The Sox9 transcription factor determines glial fate choice in the developing
928 spinal cord. *Genes & Development* 17(13), pp. 1677-1689. doi: 10.1101/gad.259003
- 929
- 930 Strelau, J. et al. 2000. Growth/differentiation factor-15/macrophage inhibitory cytokine-
931 1 is a novel trophic factor for midbrain dopaminergic neurons in vivo. *J Neurosci*
932 20(23), pp. 8597-8603. doi: 10.1523/jneurosci.20-23-08597.2000
- 933
- 934 Stuart, T. et al. 2019. Comprehensive Integration of Single-Cell Data. *Cell* 177(7), pp.
935 1888-1902.e1821. doi: 10.1016/j.cell.2019.05.031
- 936
- 937 Sun, Y. et al. 2008. Long-term tripotent differentiation capacity of human neural stem
938 (NS) cells in adherent culture. *Mol Cell Neurosci* 38(2), pp. 245-258. doi:
939 10.1016/j.mcn.2008.02.014
- 940
- 941 Supek, F., Bošnjak, M., Škunca, N. and Šmuc, T. 2011. REVIGO Summarizes and
942 Visualizes Long Lists of Gene Ontology Terms. *PLOS ONE* 6(7), p. e21800. doi:
943 10.1371/journal.pone.0021800
- 944
- 945 Takata, N. and Hirase, H. 2008. Cortical Layer 1 and Layer 2/3 Astrocytes Exhibit
946 Distinct Calcium Dynamics In Vivo. *PLOS ONE* 3(6), p. e2525. doi:
947 10.1371/journal.pone.0002525
- 948
- 949 Tcw, J. et al. 2017. An Efficient Platform for Astrocyte Differentiation from Human
950 Induced Pluripotent Stem Cells. *Stem cell reports* 9(2), pp. 600-614. doi:
951 10.1016/j.stemcr.2017.06.018
- 952

- 953 Team, R. C. 2023. : A Language and Environment for Statistical Computing. Vienna,
954 Austria: R Foundation for Statistical Computing, .
- 955
- 956 Verkhratsky, A. and Nedergaard, M. 2018. Physiology of astroglia. *Physiological*
957 *Reviews* 98(1), pp. 239-389. doi: 10.1152/physrev.00042.2016
- 958
- 959 Xin, W., Schuebel, K. E., Jair, K.-w., Cimbro, R., De Biase, L. M., Goldman, D. and
960 Bonci, A. 2019. Ventral midbrain astrocytes display unique physiological features and
961 sensitivity to dopamine D2 receptor signaling. *Neuropsychopharmacology* 44(2), pp.
962 344-355. doi: 10.1038/s41386-018-0151-4
- 963
- 964 Yun, W. et al. 2019. Generation of Anterior Hindbrain-Specific, Glial-Restricted
965 Progenitor-Like Cells from Human Pluripotent Stem Cells. *Stem Cells and*
966 *Development* 28(10), pp. 633-648. doi: 10.1089/scd.2019.0033
- 967
- 968 Zhong, S. et al. 2018. A single-cell RNA-seq survey of the developmental landscape
969 of the human prefrontal cortex. *Nature* 555(7697), pp. 524-528. doi:
970 10.1038/nature25980
- 971
- 972 Zhou, S. et al. 2016. Neurosphere Based Differentiation of Human iPSC Improves
973 Astrocyte Differentiation. *Stem Cells Int* 2016, p. 4937689. doi: 10.1155/2016/4937689
- 974
- 975 Zhu, Q., Shah, S., Dries, R., Cai, L. and Yuan, G. C. 2018. Identification of spatially
976 associated subpopulations by combining scRNAseq and sequential fluorescence in
977 situ hybridization data. *Nat Biotechnol* 36(12), pp. 1183-1190. doi: 10.1038/nbt.4260
- 978
- 979